Computer-Aided Development and Testing of Human Extra-Thoracic Airway Models for Inhalation Drug Delivery

25

Xiuhua April Si and Jinxiang Xi

Contents

X. A. Si

Department of Aerospace, Industrial, and Mechanical Engineering, California Baptist University, Riverside, CA, USA
e-mail: asi@calbaptist.edu

J. Xi (✉)
Department of Biomedical Engineering, University of Massachusetts, Lowell, Lowell, MA, USA
e-mail: Jinxiang_Xi@uml.edu

Abstract

Knowing the deposition rate and distribution of administered pharmaceuticals in the human respiratory tract is crucial to establish dose-response relationships and optimize therapeutic outcomes. Recent advances in imaging technology have made it practical to generate respiratory tract models with great details and anatomical accuracy. Pharmaceutics and inhalation drug delivery can benefit from such image-based computer-generated airway models by making available detailed information on airflow, particle motion, and wall interactions. In this chapter, we will introduce image-based computational methods to better understand respiratory aerosol dynamics. Specifically, the mouth-throat, mouth-lung, and nasal airway will be discussed. In the mouth-throat (MT) models, we will illustrate the importance of realistic airway morphologies on the accuracy of predictive inhalation dosimetry. In the mouth-lung models, experimental studies using 3D-printed hollow casts will be presented to cross-validate the predictive dosimetry models. Numerical techniques of hyper-morphing, probability analysis (including input sensitivity analysis and output uncertainty quantification), and statistical shape modeling will be introduced along the way. In the nasal model, experimental studies will be presented with different sprays, nebulizers, and delivery techniques (normal and bidirectional). New techniques that use ferromagnetic particles and pulsating flows for targeted delivery to the olfactory region and maxillary sinus will also be discussed.

Keywords

Inhalation dosimetry · CFD · Inhalation drug delivery · Respiratory dynamics

Chapter Objectives
- Demonstrate how the respiratory airway models (mouth-throat, nose, and lung) were developed.
- Explain the physics underlying pharmaceutical delivery and the numerical methods to simulate respiratory aerosol dynamics.
- Introduce the computational software and solvers used for pharmaceutical research and development, such as ANSYS Fluent and COMSOL.
- Demonstrate the computer-aided testing of the morphological effects of the upper airway on particle deposition in the mouth-throat region.
- Optimize pulmonary drug delivery using both computational modeling and in vitro experiments.
- Develop and test the nose-to-brain (N2B) drug delivery using both modeling and experimental testing.

25.1 Introduction

25.1.1 Significance of Airway Models in Pharmaceutical Development

The delivery efficiency of inhalation delivery of pharmaceutical aerosols is generally low (5–30%) and can be complicated by many factors. The human pharynx is an approximately 90° bend changing from a horizontal oral cavity to a vertical trachea. Large particles cannot maneuver through this 90° bend well very well due to their large inertia, and a large portion of them will impact onto the back wall of the pharynx and are wasted [1]. Likewise, 90% of nasal sprays will be lost in the anterior nose due to the constriction of the nasal valve as well as the large inertia of nasal spray droplets [2]. Besides the respiratory anatomical effects, inhalers and patient compliance can also affect the delivery efficiencies. In this chapter, we will focus on the effects of respiratory anatomy on inhalation drug delivery, and specifically on the effects of the flow-limiting regions such as the nasal valve, pharyngeal curvature, and glottis. In doing so, respiratory models of the nasal airway, mouth-throat model, and mouth-lung model were developed based on medical images (CT or MRI) and in vitro casts, which was explained in detail in Sect. 25.1.2.

An important factor in inhalation drug delivery is knowing where administered pharmaceuticals deposit and whether sufficient doses reach the target tissue. Both the total and locally delivered doses can be crucial to the therapeutic outcomes of the inhalation drug deliveries. Thus, it is critical to characterize aerosol deposition distributions in various respiratory regions. However, the airways are inaccessible to standard quantification and visualization instruments except for the radiological imaging approaches. However, radiological imaging also surfer from setbacks such as radioactive risk, availability, cost, and operation complexity [2, 3]. Computational predictions nowadays can approximate the in vivo conditions to high accuracies while providing tremendous details of the airflow and particles which are usually laborious to acquire in experiments. In recent years, computational simulations have gained more popularity in the design/optimization of inhalation devices and assessment of environmental health risks [4–7]. Nonetheless, drug delivery to the human respiratory tract is a complex phenomenon, which can be further compounded by numerous causes, such as patient health, respiration, device, and drug property. Large numbers of assumptions are needed to make numerical modeling feasible. As a result, many factors have to be excluded or neglected, which might have remarkably modified the transport and deposition of particles if retained otherwise. Also note that previous in vitro deposition experiments regularly used casts that were not transparent, nor could be opened apart, rendering it impractical to visualize the deposition patterns on the inner airway surfaces. It is thus highly desirable to develop techniques that can visualize and quantify the inhalation dosimetry inside the respiratory airways both accurately and simply.

The current in vitro testing of orally inhaled drug products (OIDPs) often uses a USP IP (United States Pharmacopeia induction port) followed by a cascade impactor

or a multistage liquid impinger [8]. There are attempts to quantify lung dosimetry directly from in vitro measurements. But estimations of regional dosimetry of pharmaceutical agents with the USP IP shape limited success mainly due to their underestimation of the doses in the oropharyngeal region and the subsequent overestimation in the lungs. There exists an urgent need for a new generic mouth-throat (MT) geometry in place of the USPIP to characterize the OIDP dosimetry. The USP IP has been implemented as a standard for comparison of different OIDPs and filters out the majority of large, high-speed aerosols. However, dosimetry tests with the USP IP are not satisfactory, which generally underestimates the complementary in vivo deposition data [9–11]. For the DPIs (i.e., dry powder inhalers) and pMDIs (i.e., pressurized metered-dose inhalers), mouth-throat deposition composes a large portion of the deposited dose in the human respiratory tract [12, 13]. The simple structure of the USP IP (a 90° bend with uniform circular cross-sections) fails to capture the intricate morphology of the mouth-throat airway, whose cross-sections are highly irregular in shape with variable areas. As a result, generic upper airway models with improved physical realism are needed that can predict inhalation dosimetry in the MT and lung similar to in vivo measurements. The selection of the best MT model will simulate the mean value of aerosol deposition in adult volunteers. The results will provide improved in vitro testing results for the pharmaceutical industry. A realistic human MT model will also be useful in the laboratory to study inhaled toxic particles for exposure assessment in ambient and occupational environments.

To successfully develop a generic upper airway model that is sufficiently representative of the population, we need to know the oropharyngeal factors that most affect the behavior and fates of orally inhaled drug products (OUDPs) and rank these factors according to their relative importance. However, it is inconsistent in the literature regarding such factors and their importance. Key morphological factors proposed for OIDPs include the airway volume (or the mean equivalent diameter) [14], minimum cross-sectional area [1, 15], total airway surface area [1, 16], average cross-sectional area [15, 17], airway axial length [16, 17], and oral airway curvature [1, 15, 18]. Concerning submicron aerosols, two more factors were suggested, that is, the average hydraulic diameter and the average airway perimeter of the airway [19]. Clearly, it will be ideal to know the relative importance of each factor in determining the deposition of particles of varying sizes in hope that the resultant generic airway model can capture the most important dosimetry features in most drug delivery scenarios. However, the success of inhalation drug delivery depends on the interactions between the respiratory physiology, breathing activities, medical devices, and pharmaceutical agents. Even though extensive works have been done to understand these interactions, a clear picture is still missing.

25.1.2 Previous Works

Inhalation dosimetry of orally inhaled agents can be affected by many factors, such as aerosol properties, breathing conditions, devices, and the respiratory physiology,

as demonstrated in many previous works [20–32]. Efforts in developing anatomically accurate human MT models have been undertaken based either on dental impression or medical imaging [9, 14, 17, 33–36]. Cheng et al. [33] evaluated the deposition rate of micrometer aerosols in a hollow oral cast that was reconstructed from a dental impression in a human volunteer, and the detailed dimension of these models, such as the perimeter and cross-sectional area along the main flow direction, was reported and referred to as LRRI model since then [15]. This model has been widely employed in studying the delivery efficiencies of the DPI [37] and pMDI [38]. Stapleton et al. [34] put forward an alternative but simplified mouth-throat model by retaining several physiological features like the epiglottis, variable oral size, and MT airway curvature. With this model, airflow and deposition for 3–5 μm aerosols were measured by Heenan et al. [18], revealing a strong association between the local flow characteristics and regional deposition distributions. Grgic et al. [17] demonstrated significant intersubject variability in both average and subregional depositions of OIDPs in seven MT models reconstructed from MRI scans. Efforts to quantify the intersubject variability also included Golshahi et al. [16], who tested CT-based MT and nose replicas of 6–14-year-old children. CT-based lung models were also proposed that retained lung bifurcations from G2-G9 [22, 23, 25, 39–46].

Computational fluid-particle dynamic (CFPD) simulations have been extensively used to investigate inhalation dosimetry in human upper airway models, which have been evolving from idealized, simple structures to anatomically accurate, highly sophisticated ones. Kleinstreuer and Zhang [47] developed an idealized MT model featured by a 180° bend and circular cross-sections consistent with the hydraulic diameters of the LRRI model [15]. A much higher deposition was predicted in this idealized model than the USP IP, and it is suggested that the USP IP might be inadequate to simulate in vivo dosimetry of OIDPs [48]. Xi and Longest [1] studied the effects of geometrical complexity on particle deposition using four MT models with decreasing physical realism (i.e., realistic, elliptic, circular, and constant-diameter) and demonstrated that the realistic model matched the measurements by Cheng et al. [15] better than the three idealized models. Furthermore, large discrepancies in the local or cellular-level deposition were predicted among MT models with varying levels of complexities, which could be one order of magnitude higher in the realistic MT model than in the idealized geometries. The triangular glottal aperture and the dorsal-sloped trachea were found to significantly enhance the deposition in the realistic model. Geometrical details are needed to assess the formation of deposition hot spots that are essential in accurately estimating the tissue response at the cellular level. Considering that the elliptic model retained key geometrical factors and can reasonably capture the deposition variations, it has been applied to investigate the deposition of DPI aerosols in the upper airway and was later labeled as the VCU (Virginia Commonwealth University) model [49, 50].

Validated methods exist for the measurement of inhalation dosimetry in respiratory airway hollow casts [51, 52]. By contrast, methods to visualize and quantify regional or local deposition fractions have rarely been reported. Dye-based approach with methylene blue can visualize the regional drug bioequivalence in terms of the

intensity of the blue stain [53]. However, this method cannot quantify the dosage and the deposited dye can drip and diffuse. Gamma scintigraphy using technetium-99m (^{99m} Tc) agents have been used to envisage drug distributions in the human noses both in vivo [54–56] and in vitro [57–59]. One setback of this method is that the gamma rays attenuate quickly in the human body and up to 50% energy can be scattered by the body tissue [60]. Such energy scattering can also distort the resultant images and give rise to biased dosimetry [61]. Besides, scintigraphy images are 2D and cannot distinguish deposition in different depths. Kundoor and Dalby [62, 63] demonstrated the utility of a simple, effective method to visualize droplet deposition patterns using Sar-Gel, a water-sensitive paste (Sartomer Arkema Group, Exton, PA) that turns into red upon water contact. Sar-Gel is highly sensitive to liquid water and can detect deposited water as low as 0.5 μL in volume, which is about the size of the smallest droplets in nasal sprays. Moreover, color spreading occurs only when the volume of a single droplet exceeds 25 μL. In light of other advantages like short reaction time, safe, and easy cleanup, Sar-Gel is well suited for the visualization of particle deposition.

Variability in the pulmonary drug delivery efficiency can result from different factors such as patient airway structure, respiration condition, device usages, and drug properties [64, 65]. Certain sources can be hard to control and will considerably alter drug delivery efficiency and therapeutic outcome consistency. Unfortunately, deterministic models cannot take into account the inherent uncertainties of the inputs directly [66–68]. Considering the increasing demand for reliable quantification of inhalation dosimetry, alternative models are needed that can determine the output uncertainty but are still numerically efficient. To meet these challenges, we combined two distinct methods, that is, the deterministic models [69–71] and the probabilistic analyses including the sensitivity analysis and uncertainty quantification [72, 73]. Valuable information can be yielded regarding the reliability (or confidence level) of the estimated dosimetry [74].

Most previous studies have excluded the input probability distributions in estimating the intersubject dosimetry variability; instead, variability was considered by comparing different input parameter values or between different airway geometries, and thus was still deterministic. One exception was Guo et al. [75], who used Monte Carlo simulations to estimate the propagation of input uncertainties in nasal sprays. They concluded that the regression approach and resulting standard deviations overestimated the output uncertainty, and Monte Carlo simulations could predict statistically significant confidence levels. The setback of the Monte Carlo method required prohibitive computational resources to solve the fluid-particle dynamics in a large number of test cases for statistical analysis. There exist more efficient sampling methods, such as the response surface method (RSM) and the algorithm of most probable point (MPP) [74]. Probabilistic analysis for the dosimetry of pulmonary drug delivery has been scarce.

The objective of this chapter is to introduce the fundamental theory and principles behind the inhalation drug delivery, as well as the latest advances in the computer-aided development of human upper airway models and their applications in aerosol inhalation dosimetry. Both numerical simulations and in vitro experiments will be

presented. It is hoped that this chapter will provide a comprehensive introduction to respiratory aerosol dynamics for the general audience and at the same time provide a review of state-of-the-art techniques for active practitioners in this field. Specific objectives include:

1. Demonstrate how the respiratory airway models (mouth-throat, nose, and lung) were developed.
2. Explain the physics underlying pharmaceutical delivery and the numerical methods to simulate respiratory aerosol dynamics.
3. Introduce the computational software and solvers used for pharmaceutical research and development, such as ANSYS Fluent and COMSOL.
4. Demonstrate the computer-aided testing of the morphological effects of the upper airway on particle deposition in the mouth-throat region.
5. Optimize pulmonary drug delivery using both computational modeling and in vitro experiments.
6. Develop and test the nose-to-brain (N2B) drug delivery using both modeling and experimental testing.

25.2 Methods

25.2.1 Computer-Aided Development of Airway Models

25.2.1.1 Mouth-Throat Model

We will use three examples to demonstrate the methods to reconstruct surface geometries of the human airway from either preexisting casts or on-shelf medical images (i.e., CT or MRI scans). Figure 25.1 illustrates the procedures of developing a mouth-throat model. The oral airway was developed from a dental impression with a half-way mouth opening. Detailed dimensions of the slices along the airway (second panel in Fig. 25.1a) such as cross-sectional shapes, perimeters, areas, and hydraulic diameters were provided in Cheng et al. [33]. The shape and dimension of the contours followed those measured in Cheng et al. [33]. These contours were then connected with smooth lines, and faces were built to cover the entire mouth cavity, giving rise to the realistic model as shown in the third panel of Fig. 25.1a. The throat model was developed from the CT images of a healthy adult that was acquired at a resolution of 1 mm. The software package MIMICS (Materialise, Leuven, Belgium) was applied to convert CT scans to a solid body model. The combined mouth-throat (MT) model was then imported as an IGES file into the software ANSYS ICEM CFD (ANSYS, Inc., Canonsburg, PA) for meshing. Geometric surface smoothing was conducted to remove artifacts or unnecessary anatomical details to avoid excessive grid elements. Major characteristics retained in this realistic MT model include a half opening mouth, a realistic MT airway curvature, a triangular glottal aperture, and a sloped upper trachea (Fig. 25.1a). Landmark structures like the mouth opening, larynx, and trachea were scaled to match the reported data in
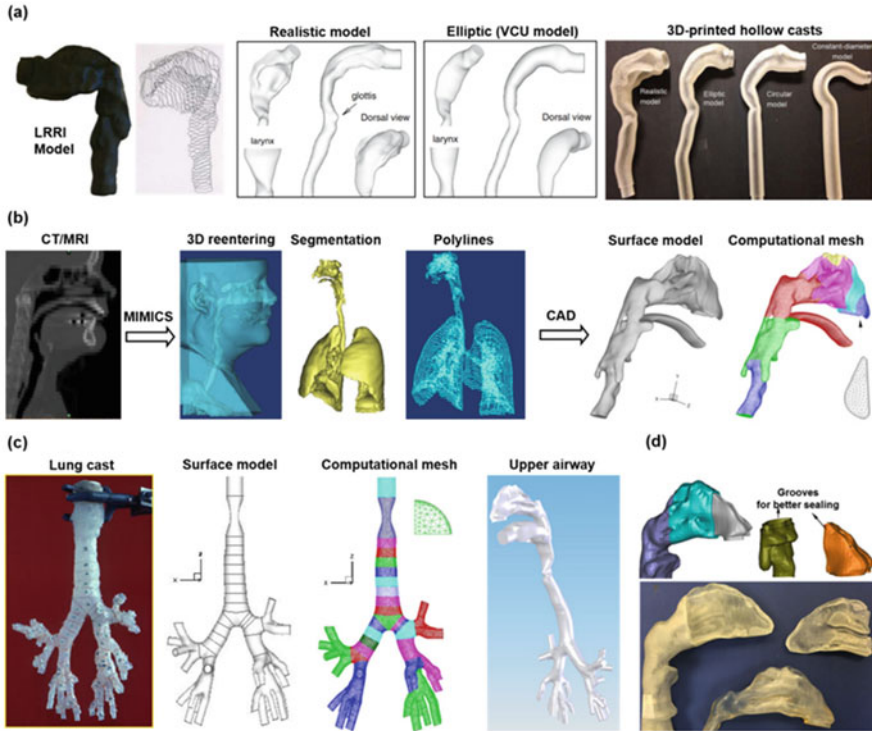
Fig. 25.1 Airway model reconstruction: (**a**) mouth-throat (MT) model that was based on the LRRI (Lovelace Respiratory Research Institute) model, (**b**) nasal model reconstructed from CT scans, and (**c**) lung model reconstructed from the lung cast provided by Dr. Cohen at New York University. The three parts have been combined to form a complete extra-thoracic airway model. Computational meshes were generated using the meshing software ANSYS ICEM CFD for numerical analysis and hollow casts were fabricated using 3D printing techniques for in vitro tests. Step grooves were developed at each interface for easy assemble and good sealing, as shown in (**d**). The elliptic MT model has evolved into the current VCU model

previous deposition studies, leading to a mouth opening diameter of 2.2 cm, a glottal area of 0.87 cm^2, and a tracheal area of 2.0 cm^2 (Fig. 25.2a).

In the first step of simplification, the cross-sections of the realistic model were replaced with ellipses of the same hydraulic diameters (Fig. 25.1). The resulting elliptic model is much simpler by removing the anatomical details of the cheek-teeth lumen and replacing the triangular glottis using an oval glottal aperture. This elliptic model has evolved into the current VCU model, as widely accepted in pharmaceutical industries [49, 50]. Further simplifications were made to generate the circular and constant-diameter models, as illustrated in the right panel of Fig. 25.1a. In the circular model, all cross-sections are circular with equivalent hydraulic diameters to those in the realistic and elliptic models. The constant-diameter model consists of a 180° bend (curvature radius: 3.2 cm) of a constant-diameter tube (area: 4.43 cm^2).
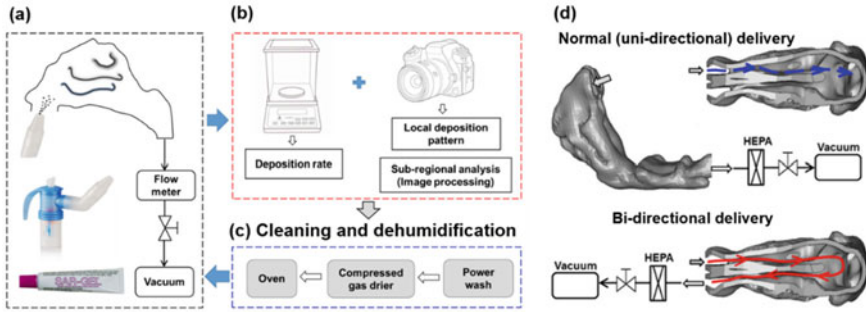
Fig. 25.2 Intranasal deposition test diagram: (**a**) drug delivery testing platform with a vacuum pump to simulate steady-state nasal inhalation, (**b**) dosimetry and distribution analyses, (**c**) cast cleaning and dehumidification, and (**d**) two delivery strategies: normal (or unidirectional) and bidirectional

The airway volumes of the four models (i.e., realistic, elliptic, circular, and constant-diameter) are 65.1, 56.8, 52.5, and 35.4 cm³, respectively.

25.2.1.2   Nasal Model

The second example shows the reconstruction of a nasal model from MRI head scans of a 53-year-old male with no known respiratory diseases (Fig. 25.1b). This image data were originally reported in Guilmette et al. [76] and had since then been used in several in vitro tests [77–80] and numerical simulations [69, 81–85]. MIMICS (Materialise, Leuven, Belgium) was used to convert the image data set into a solid airway model, which was further converted into a group of polylines defining the solid model. From these polylines, a surface geometry was reconstructed using Gambit (ANSYS, Inc., Canonsburg, PA) (Fig. 25.1b). The boy-fitted mesh was generated for the nasal model, with five layers of prismatic cells in the near-wall region (right panel, Fig. 25.1b).

25.2.1.3   Lung Model

The third example shows the reconstruction of the lung. The original lung cast had been developed postmortem from a 34-year-old male [86] and was scanned using a Discovery LSCT scanner (GE Medical Systems) with 512 × 512 pixel resolution, 0.7-mm slice spacing, and 0.65-mm overlap. Acquired scans were segmented using MIMICS (Materialise, Leuven, Belgium) into a solid geometry and its defining polylines, from which a surface geometry was reconstructed using Gambit (ANSYS, Inc., Canonsburg, PA). The resulting lung geometry extends from the trachea to the bifurcation generations four to six (G4-G6). In total, there are 23 outlets and 44 bronchi retained.

The three regions of the respiratory tract (mouth-throat, nose, and lung) were also connected into one model (right panel in Fig. 25.1c). Computational meshes can be generated using ANSYS ICEM CFD (Canonsburg, PA) for numerical analysis. Similarly, hollow casts can be fabricated from these models for in vitro deposition

tests. Figure 25.1d shows the nasal airway casts built with an in-house 3D printer (Stratasys Objet30 Pro, Northville, MI). The casts have a uniform wall thickness (4 mm). The 3D the printing resolution is 16 μm (0.0006 in) and the printing material is polypropylene (Veroclear, Northville, MI).

25.2.2 Experimental Setup

Figure 25.2 illustrates the experimental setup for nasal deposition tests with three steps: drug administration, deposition analysis, and cast cleaning and dehumidification. Steady inhalation was simulated using a vacuum (Robinair 3 CFM, Warren, MI) connecting to the nasopharynx. A flow meter (Omega, FL-510, Stamford, CT) was utilized to monitor the volumetric flow rate (Fig. 25.2a). Before testing, the inner walls of the nasal airway cast were coated with a thin layer of Sar-Gel and then put together and fastened with a clamp. A high-precision electronic scale (Sartorious, 0.01 mg precision, Elk Grove, IL) was employed to measure the weight of the nasal cast (W_0), as illustrated in Fig. 25.2b. Aerosols were released into the nostrils for a specified time (e.g., 20 s) at 30° from the vertical orientation [63]. In the second step (immediately after the aerosol release), the new weight (W_1) of the cast was measured. The added weight ($\Delta W = W_1 - W_0$) denoted the deposited aerosols, and the deposition fraction was computed as ΔW over the output from the spray/ nebulizer. The cast was then disassembled and photos were taken of the Sar-Gel color on the inner walls (Fig. 25.2b). In the third step, a power washer (Karcher, 1600 psi, West Allis, WI) was used to wash away the Sar-Gel on the cast surface (Fig. 25.2c). To remove the moisture, the cast was positioned in an oven (ThermolyneFurnatrol*18200*, Dubuque, IA) at 55 °C for 60 min. The cast was then left in the lab for another 60 min to allow the relative humidity and temperature of the cast to become fully equivalent to the environment. The third step was essential in the deposition measurement to avoid the complication from hygroscopic effect (dry surface) or water evaporation (wet surface), both of which could lead to fluctuations of the electronic scale reading. In nasal drug delivery, two strategies were presented, with one being the normal, unidirectional approach, where drugs were released into one nostril and inhaled into the lung, and the other being bidirectional, where drugs were released into one nostril and exited via the other nostril, as shown in Fig. 25.2d.

25.2.3 Computational Fluid-Particle Governing Equations

Respiration airflows were assumed to be Newtonian flows, incompressible, and isothermal. The low-Reynolds k-ω turbulence model was adopted to resolve the flow field [52, 83, 87]. The trajectories of particles were tracked using the discrete-phrase Lagrangian approach [85]. The general governing equation of particle motion is:

$$\frac{d(m_\mathrm{p} v_i)}{dt} = \frac{f}{\tau_\mathrm{p} C_\mathrm{c}} m_\mathrm{p}(u_i - v_i) + m_\mathrm{p} g_i(1 - \alpha) + F_{i,\mathrm{Lift}} + F_{i,\mathrm{Brownian}}$$
$$+ F_{i,\mathrm{Magnet}} + F_{i,\mathrm{Acous}} \tag{25.1}$$

where u_i and v_i are the velocity of the airflow and particle, respectively, τ_p (i.e., $\rho_\mathrm{p}\, d_\mathrm{p}^2/18\mu$) is the particle reaction time to airflow, C_c is the Cunningham slip correction factor, and f is the drag calculated following Morsi and Alexander [88]. The Saffman lift force was also included for micrometer particles and the Brownian motion force was included for nanoparticles [89]. Also, the magnetophoretic force can be considered for magnetic particles and acoustic force for pulsating aerosols.

25.2.3.1 Magnetophoretic Force

The magnetic flux density B depends on the permeability of free space μ_0, the magnetic intensity H, and the magnetization M [90]:

$$B = \mu_0(H + M) \tag{25.2}$$

The effective magnetic dipole moment caused by H is calculated as:

$$m_\mathrm{eff} = \frac{4}{3}\pi d_\mathrm{p}^3 K H \tag{25.3}$$

Here, K is the Clausius-Mossotti factor $K = (\mu_\mathrm{p} - \mu_\mathrm{f})/(\mu_\mathrm{p} + 2\mu_\mathrm{f})$. The magnetophoretic force exerted on a spherical particle in a nonuniform magnetic field is [91]:

$$F_{i,\mathrm{Magnetophoretic}} = (\mu_0 m_\mathrm{eff} \cdot \nabla)H \tag{25.4}$$

The symbols μ_p and μ_f are the magnetic permeability of particles and fluid, respectively. From Eqs. 25.3 and 25.4, the magnetophoretic force is proportional to the particle volume, and the product of the magnetic field and its gradient. The direction of the force is along the magnetic field gradient.

25.2.3.2 Acoustophoretic Force

For the pressure acoustic computation, boundary conditions are the sound hard boundary for the wall, the plane wave radiation for the outlet, and the pressure for the inlet. The governing equations to calculate the acoustophoretic force is shown below [92]:

$$f_{i,\text{acoust}} = -\nabla\left[V_{\text{p}}\left(f_1\frac{P^2}{2\rho c^2} - f_2\frac{3}{4}\rho v^2\right)\right]; \ \ f_1 = 1 - \frac{k_0}{k_{\text{p}}}; \ \ f_2$$

$$= \frac{2(\rho_{\text{p}} - \rho)}{2\rho_{\text{p}} + \rho} \tag{25.5}$$

Here ρ is the air density, ρ_{p} is the particle density, V_{p} is particle volume, v is particle velocity, P is the instantaneous pressure, k_0 and k_1 are the bulk moduli, and f_1 and f_2 are the scattering coefficients for the monopole and dipole, respectively. Multiphysics software COMSOL (Burlington, MA) was implemented to simulate the pulsating pressure distributions and associated particle motions.

25.2.4 Numerical Methods

Both ANSYS Fluent (Canonsburg, PA) and COMSOL (Burlington, MA) were used to resolve the airflow and track the particle motions. In ANSYS Fluent, user-defined functions (UDFs) were developed to consider the near-wall velocity interpolation (NWI) and anisotropic turbulent effect. Near-wall interpolation is a linear function of the particle velocity from zero at the wall to the velocity at the cell center. Second-order spatial discretization or higher were used for all transport terms. The convergence of airflow solution was achieved when the mass residual decreased by five orders of magnitude and the residual variation profiles for both mass and momentum became flat. Convergence sensitivity analyses were also conducted to establish grid-independent and particle-count-independent results following the method of Xi et al. [93].

The computational mesh of respiratory models was created with ANSYS ICEM CFD (Canonsburg, PA) with tetrahedral cells in the main flow region and body-fitted multi-layer prismatic cells in the near-wall region. It has been demonstrated that the near-wall prismatic cells are critical in establishing grid-independent results. To achieve a similar level of numerical accuracy, the total number of cells needs to be five times higher in the all-tetrahedral mesh than a hybrid tetrahedral mesh with near-wall prismatic cells [89].

25.2.4.1 ANSYS Fluent and ICEM CFD

ANSYS Fluent (Canonsburg, PA) is a popular engineering software to simulate fluid flow, heat transfers, fluid-structure interactions, aeroacoustics, and electromagnetic flows. The latest version is ANSYS Fluent 2020R2. Due to its high accuracy and robustness, ANSYS Fluent has been widely used in both academia and industries. In recent years, ANSYS Fluent has been providing a student version, which is freely available to all students in the world. This version can be installed on any Microsoft Windows 64-bit machine. This product can be downloaded via the link: https://www.ansys.com/academic/free-student-products. Examples of using ANSYS Fluent in pharmaceutical design and delivery can be found in [94–96].

ANSYS ICEM CFD (Canonsburg, PA) is the mesh generation software bundled with ANSYS Fluent. It can efficiently mesh large, complex models with either structured or unstructured elements. ANSYS ICEM CFD can read geometries generated in most computer-aided design software, such as Gambit, Solidworks, CATIA, blender, etc. The geometry format include step, IGES, sat, xml, STL, VRML, and other third-party mesh format. The generated mesh can be exported for either computational fluid dynamics or finite element analysis. More information about ANSYS ICEM CFD can be found in: https://www.ansys.com/services/training-center/fluids/introduction-to-ansys-icem-cfd.

25.2.4.2 COMSOL Multiphysics

COMSOL Multiphysics (Burlington, MA) is a computation software that gains popularity in recent years due to its easy-to-use features and its capacity in simulating multiple physics. As of November 2020, the latest version is COMSOL 5.6. COMSOL was started as "FEMLAB" around 20 years ago and took root in the finite element method to solve engineering problems. The software was later changed to the current name. COMSOL does not provide free, student version. The trail period is generally 15 days. The software comprises the base module to conduct general engineering simulations, as well as a variety of specialty modules to tackle specific physics, such as electrical, mechanical, particles, acoustics, and chemical applications. The system requirements for installation include at least 4 GB of RAM and 2–13 GB of disk space, depending on your installation options of specialty modules.

The physics included in the software covers almost all aspects of engineering. Besides electric problems (or AC/DC: alternating current/direct current), it also includes magnetic, acoustic, solid mechanics, flow, heat, and chemical applications. COMSOL's interface allows the user to include different physics easily. Another salient feature is that there are a large number of tutorials that are readily available to new users to start, either in the library embedded with the software or through the gallery of the COMSOL website: https://www.comsol.com/models. Either new users with no prior experience with COMSOL or experienced users can learn from these tutorials. The Fluid-flow module and particle-tracing module are the two modules needed to study the transport and deposition of pharmaceutical particles. If there are electrostatic charges in the particles, AC/DC module should be used. For those who are interested in product designs of inhalers, the optimization module is also needed. For readers who are interested in learning more about this software, please refer to https://www.comsol.com/comsol-multiphysics. Interested readers are also referred to a video tutorial that explains step by step how to COMSOL and ANSYS Fluent to simulate olfactory drug delivery with active control of pharmaceutical aerosols [97]. More examples can be found in [98, 99].

25.2.5 Statistical Analysis

Statistical analysis software Minitab (State College, PA) was utilized to evaluate the variance in dosimetry. To assess the sample variability and determine the major influencing factors, one-way analysis of variance (ANOVA) and Tukey's method with stacked data were applied. To compare the relative importance between different factors, the mean effect analysis of ANOVA was performed, for example, on the MT model, particle size, geometrical factor, and inhalation rate [100]. To evaluate the interactive effects of dominating factors, the interaction analysis of ANOVA was undertaken. When the p-value was <0.05, a statistically significant difference was reached.

25.3   Applications

25.3.1 Model Validation

The computational models of the nasal, mouth-throat, and mouth-lung geometries had been extensively validated, as demonstrated in Fig. 25.3a–c, respectively. All models were meshed with five layers of prismatic elements near the wall, as illustrated in the left panel in Fig. 25.3a. Near-wall grid convergence was established at the near-wall height of 0.05 mm for both 150 nm and 1 m particles (middle panel,
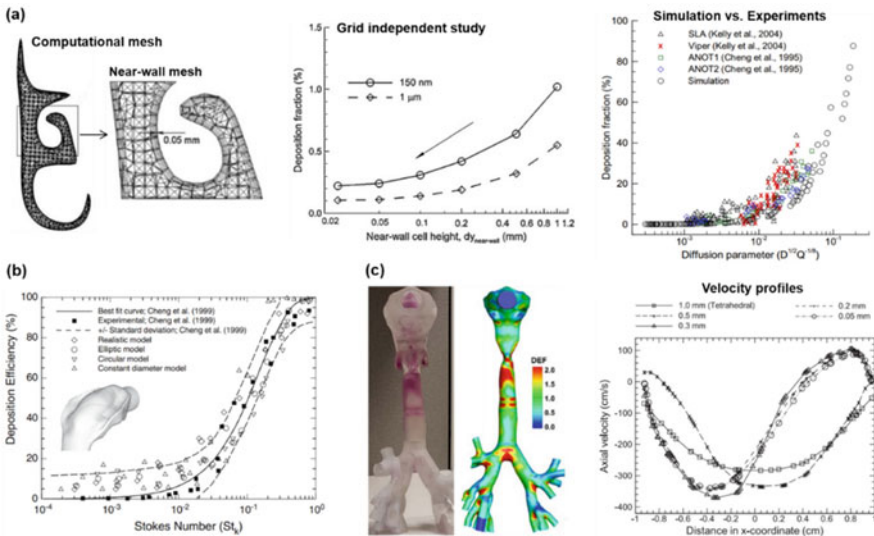
Fig. 25.3 Validation for the nasal, mouth-throat (MT), and mouth-lung models: (**a**) computational mesh, grid-independent study, and simulation versus experiment, (**b**) MT model validation for micrometer particles as a function of Stokes number, and (**c**) mouth-lung model validation in terms of deposition visualization, and velocity profile variation versus mesh density

Fig. 25.3a) for the nasal cavity. Further refining the near-wall cells below 0.05 mm was demonstrated to have a small effect on the deposition rate. The third panel in Fig. 25.3a shows the comparison of the CFD-predicted deposition fractions and in vitro test results versus a diffusion parameter proposed by Cheng et al. [15].

Figure 25.3b shows the numerically predicted deposition rates versus the particle Stokes number for the four mouth-throat models as shown in Fig. 25.1a in comparison to measured data and Cheng's empirical correlation in the LRRI (Lovelace Respiratory Research Institute) MT model [15]. Nearly all predicted data from the four MT models fall within the experimental uncertainty bonds. In particular, the most idealized constant-diameter model (triangles) overestimated the in vitro data.

Deposition visualization was also used for model validation purposes, as illustrated by Fig. 25.3c. It was observed that the numerical predictions matched the experimentally determined deposition distribution to a high degree, suggesting that the computer models indeed captured the particle behaviors and fates. In particular, we observed several positions where the predictions and measurements are highly similar. For instance, the computer model successfully captured the crescent deposition hot spot immediately downstream of the glottis. Moreover, there were two streaks in the front middle trachea in both the predicted and experimental deposition patterns.

Mesh sensitivity analysis of the airflow velocity field is presented in the right panel of Fig. 25.3c, which compares the velocity profiles between different mesh densities in the tracheal mid-plane 3 cm below the glottis. Large discrepancies in the velocity profiles exist between coarse and fine near-wall heights, indicating that the airflow is highly sensitive to the near-wall grid size. Moreover, the velocity profiles in the two coarsest meshes (near-wall height: 1.0 and 0.5 mm) were relatively symmetric. By contrast, the velocity profiles became more asymmetric with increasingly finer meshes. It appeared that the coarse meshes failed to capture the skewed or reversed flows because of exceeding numerical diffusion. From Fig. 25.2, the convergence for the velocity field was achieved at the near-wall height of 0.05 mm. The good agreement between model simulations and experiments in both the deposition rate and deposition distributions, as well as the grid-independent airflow field, imparts confidence into the subsequent simulation results.

25.3.2 Mouth-Throat Model Development and Testing

Figure 25.4a shows the dimensions of different MT models in terms of perimeters and hydraulic diameters versus the axial distance from the oral opening. As expected, the largest variability was observed in the realistic model in all geometrical parameters. Dimension discrepancies between the realistic and elliptic models are due to the removal of the cheek-teeth cavities in the realistic MT model. The second panel shows the airflow fields (i.e., velocity vectors, mid-plane contours, and streamlines) in the realistic and constant-diameter MT models at 30 L/min. In the realistic model, the peak velocity downstream of the glottis (i.e., laryngeal jet) shifts to the front wall of the trachea due to fluid inertia (Fig. 25.4b, right panel). This jet
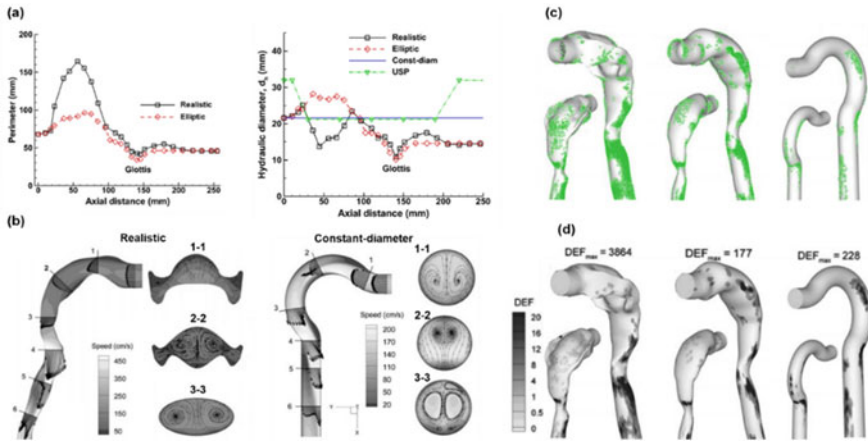
Fig. 25.4 Geometrical complexity effects of the mouth-throat (MT) models: (**a**) perimeter and hydraulic diameter of the MT models, (**b**) airflow patterns in the realistic and constant-diameter models, (**c**) surface deposition of 6 μm particles, and (**d**) local deposition in terms of the deposition enhancement factor (DEF)

effect induces reversal flows near the back wall of the trachea. Considering the sloped angle of the trachea in the realistic and elliptic models, increased particle impaction is expected from the laryngeal jet. In the constant-diameter model (Fig. 25.4b), a pair of counter-rotating helical vortices are observed in most cross-sections, which are absent in the realistic model. Due to a different curvature than that in the realistic model, the maximum velocity in the constant-diameter model is observed near the upper wall instead of the lower concave surface as in the realistic model (Fig. 25.4b).

A comparison of deposition distributions is shown in Fig. 25.4c, where both the deposition rate and distribution differ significantly among MT models with varying physical realism. For the realistic and elliptic models, elevated deposition is observed in the back of the pharynx due to the abrupt MT curvature and associated particle inertia impaction. By contrast, reduced deposition is observed throughout the pharynx in the constant-diameter model (right panel, Fig. 25.4c). Large variations in deposition distributions are found at other locations too, including the lower larynx and trachea. Specifically, high levels of particle accumulation occur in the realistic model below the glottis (right panel, Fig. 25.4c); however, the intensity of this particle accumulation decreases as the geometrical complexity decreases from the elliptic to the constant-diameter models.

To further investigate the impact of the geometrical factors on inhalation dosimetry [100], the shape of existing MT models was modified using Hypermorph, as illustrated in Fig. 25.5a. One advantage of Hypermorph is that geometry can be modified locally in a quantitative manner (Fig. 25.5b), and thus is well suited for a systematic parameter study. Figure 25.5c displays the modified realistic and elliptic MT models with three factors of interest: oral cavity volume, glottal aperture, and
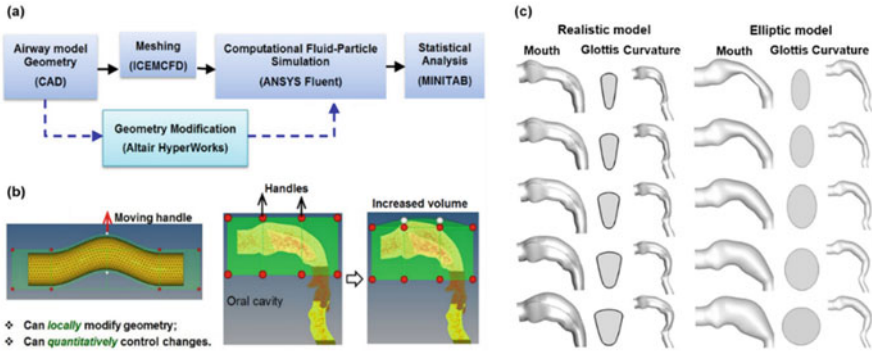
Fig. 25.5 MT model modification: (**a**) flowchart showing the airway models being systemically modified for subsequent parametric studies, (**b**) using Hypermorph to modify a model geometry locally and quantitatively, and (**c**) modified MT geometries for the realistic and elliptic models with varying oral cavity volumes, glottis areas, and MT curvatures. The effect of total airway volume was evaluated by uniformly scaling the MT models with four different scale factors (not shown due to unchanged shape)
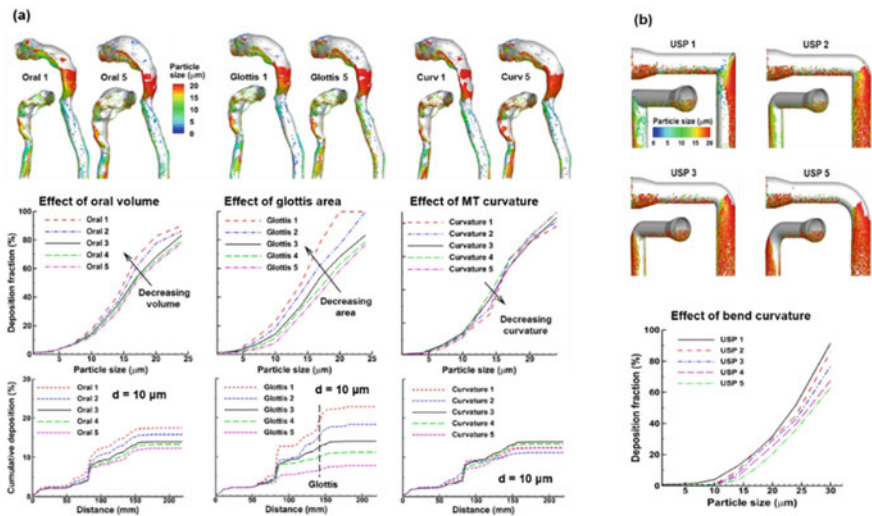
Fig. 25.6 Deposition variations in modified geometries: (**a**) USP and (**b**) realistic models. In USP, the effect of bend curvature on surface deposition and deposition fraction is shown at 30 L/min

airway curvature. The effect of total airway volume was also evaluated by uniformly scaling the MT models with four different scale factors, but figures were not shown due to unchanged shape.

Figure 25.6a shows the differences in deposition among the modified realistic geometries at 30 L/min in terms of (1) oral cavity volume, (2) glottal aperture area, and (3) airway curvature. These included the deposition pattern (upper panel), the
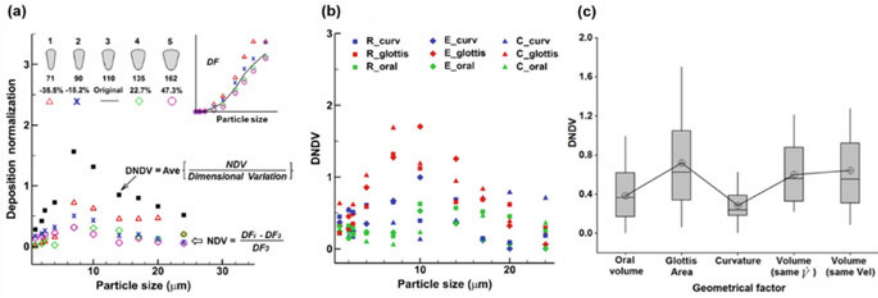
Fig. 25.7 Sensitivity analyses of the geometrical factors: (**a**) dimensionally normalized deposition variation (DNDVs); (**b**) DNDV versus particle size in three different MT models in realistic (R), elliptic (E), and constant-diameter (C) model geometries; and (**c**) box plots of DNVCs for different geometrical factors

deposition rate (middle panel), and the cumulative deposition fractions of 10-µm particles along the mean flow direction (lower panel). When varying the above three factors, deposition changed much differently in both magnitude and trend. For instance, reducing the glottal area and oral volume both increased the deposition fractions; by contrast, reducing the MT curvature (in both length and angle) decreased particle deposition (Fig. 25.6a, right panel). In this example, the most influencing factor was the glottal area, followed by the oral volume, while the impact from the MT curvature was the least among the three factors. Variations in the glottal area led to significant changes in particle deposition both before and after the glottal aperture (Fig. 25.6a).

Figure 25.6b displays the deposition patterns in the modified USP ducts by replacing the sharp 90° bend with smoothed ones of varying curvatures. The reduced deposition was predicted in the curved bend in comparison to that in the sharp bend, as expected. The USP deposition further decreased with increasing curvature radius, presumably resulting from smoother particle trajectories and diminished inertial impactions (Fig. 25.6b). In smoothed USP ducts, fewer particles were deposited on the back of the bend and more on the ventral and lateral sides.

To assess the impacts from the geometrical factors, the deposition variations, instead of the absolute deposition rate, were considered, which were first normalized by the control case deposition rate, and then by the magnitude of the dimensional variation, that is, dimensionally normalized deposition variation (DNDVs). Figure 25.7a shows the deposition normalization with respect to the glottal area in the realistic model. There are five variants of glottal apertures (Case 1–5) and Case 3 (original dimension) was used as the control case. Figure 25.7b shows the resultant DNDV in terms of the particle size in the realistic (R), elliptic (E), and constant-diameter (C) model geometries. The DNDV denotes the relative change in deposition per unit structural variation. To determine the major influencing factors, the DNDVs for all variables considered (geometry variation, particle size: 0.5–24 µm, and breathing condition: 15–60 L/min) were analyzed by means of ANOVA. Figure 25.7c shows the box plot of the five influencing factors. The glottal aperture

area and the airway volume were the most important factors in determining MT dosimetry of micrometer particles, while the oral volume and the MT curvature exerted an insignificant impact. Note that the "*volume*" in Fig. 25.7c represented the entire MT airway, as opposed to the oral volume. Two breathing conditions were considered when considering the MT volume effect: the same inlet velocity and the same inhalation flow rate. From Fig. 25.7c, the MT volume effect was observed to be significant (p-value <0.01) in both scenarios.

25.3.3 Pulmonary Drug Delivery

25.3.3.1 Probability Analysis

The dosimetry uncertainty was evaluated due to variability in three inputs: particle size, particle density, and inhalation flow rate (Fig. 25.8a). The input variability of each input variable has a normal distribution and a standard deviation σ that is 25% of the mean μ. Figure 25.8b shows the dosimetry variability at a 95% confidence level based on the prescribed input uncertainties.

A comparison of the input sensitivity of the three factors is illustrated in Fig. 25.8c in terms of mean and total effects. The index of the main effect represents a variable's individual impact on the response, while that of the total effect includes both the main effect index and the interactions with other influencing parameters [101]. As a result, the disparity between these two indexes is from the interactions among the inputs. For both indexes, the variability in particle size is the most sensitive factor in determining the pulmonary dosimetry, while the variability in the airflow speed is the least among the three factors. Interestingly, even though the airflow speed has a very small main effect, it still affects the pulmonary dosimetry by its strong interactions with other parameters, as shown by the relatively larger total effect (Fig. 25.8c). Only a parameter that has a near-zero total-effect index should be considered to be trivial.
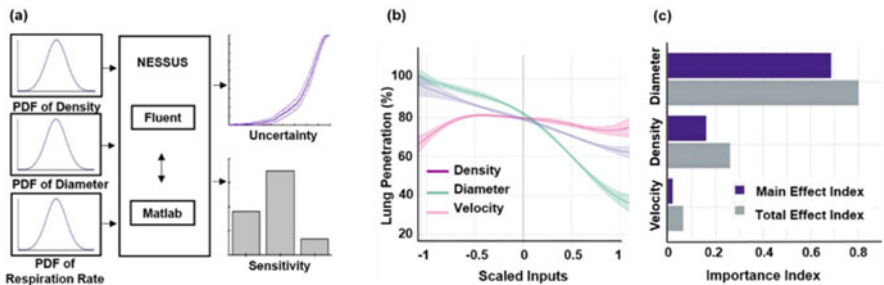

Fig. 25.8 Probability analysis of deposition in the mouth-lung model: (**a**) the flowchart of probability analysis that combines NESSUS, ANSYS Fluent, and Matlab, with normal distributions of particle density, particle diameter, and inlet airflow velocity; (**b**) dosimetry uncertainty at 95% confidence level; and (**c**) input sensitivity of the three factors

25.3.3.2 Deposition Visualization: CFD Versus Experiments

Both numerical simulations and in vitro experiments were conducted in the mouth-lung model (Fig. 25.9a). Complex flow fields arose from the complex airway structures, as shown in Fig. 25.9b. Salient features included an abrupt (90°) change in the main flow direction, a laryngeal jet, and flow instability downstream of the glottis [102]. Significant inertial deposition in the velopharynx dorsal wall was expected from the abrupt change in the flow direction (Slice 1, Fig. 25.9b).

The laryngeal jet induced a flow recirculation zone in the upper trachea, which could increase the resident time of particles in this region and thereby increase particle deposition (Slice 3, Fig. 25.9b). Considering the coherent structures, stream-wise vortex filaments formed above the glottal aperture from secondary swirling flows and continued to grow because of the energy inputs from the laryngeal jet, inducing vortex rings within the upper trachea. These coherent structures had a direct impact upon the generation and decay of turbulence, as well as the pressure drop across the glottal aperture. Considering the aerosol transport (right panel in Fig. 25.9b), the majority of particles were found to follow the high-speed main flow and fewer particles were found in the low-speed or recirculation regions. Aerosols reached the lung carina ridge about $T = 0.16$ s after being inhaled.
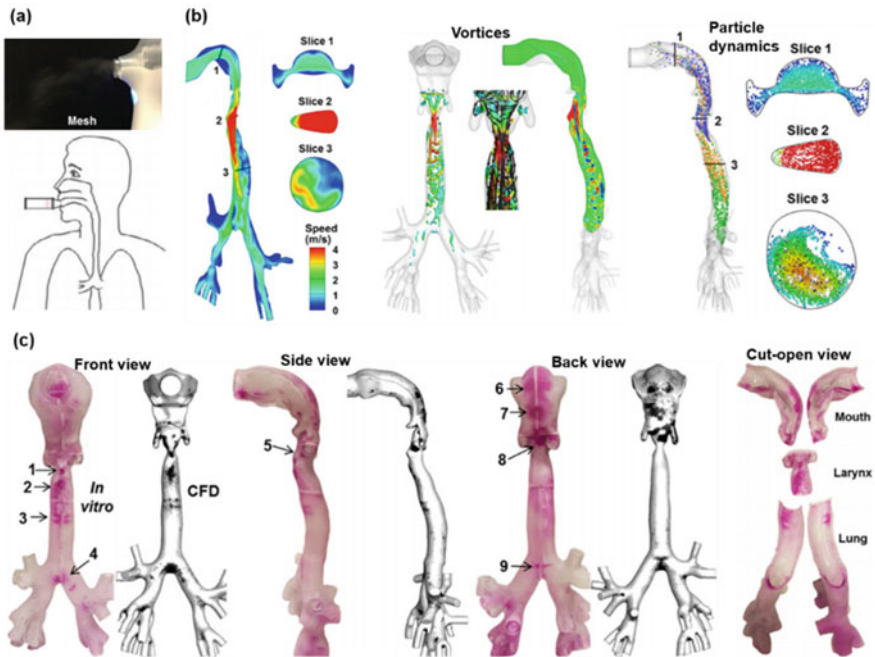
Fig. 25.9 Comparison of in vitro measurements and computational predictions in a mouth-lung cast under normal breathing condition: (**a**) in vitro experimental diagram; (**b**) computationally predicted airflow, vortex coherent structures, and particle dynamics; (**c**) experimental measurements versus CFD predictions of the particle deposition distribution in the front, side, back, and cut-open views

Due to the laryngeal jet, particles were shifted to the ventral wall of the trachea (Slice 3, right panel, Fig. 25.9b). As a result, enhanced particle depositions were expected in the ventral wall of the trachea, which was corroborated by the Sar-Gel visualizations shown in Fig. 25.9c.

Figure 25.9c compares side by side between the in vitro experiments and computational predictions of deposition distributions of nebulized aerosols at 30 L/min, which closely resembled each other and validated the computer models hereof in capturing the particle behaviors and fates in human airways. In particular, Fig. 25.9c listed nine locations, where CFD and Sar-Gel visualization compared favorably [102]. These included the deposition hot spots at the glottis tip (point 1), downstream of the glottis (point 2), middle trachea (two strips, point 3), front of the lung carina ridge (point 4), lateral larynx (point 5), the roof of the oral cavity (points 6, 7), dorsal pharynx (point 8), and back of the carina ridge (point 9, Fig. 25.9c). A cut-open view of the aerosol deposition in the mouth-lung model is illustrated in Fig. 25.9c. Since the aerosol depositions on the inner walls are directly exposed and are not biased by the transparency of the casts, Fig. 25.9c provides a more accurate representation of the delivered pharmaceuticals inside the airways. In addition, as the Sar-Gel color depth depends directly on the mass of the applied water, delivered doses can be quantified, as demonstrated in Xi et al. [2].

25.3.3.3 Deposition Visualization: Normal and Diseased Breathing Conditions

Various lung compliance and airflow resistor (PneuFlo Parabolic) were used varied in the breath simulator to simulate diseased breathing conditions (Fig. 25.10a). For instance, to simulate asthmatic respiration, the default resistors for normal breathing Rp 5 (i.e., 5 cm H_2O/L/s) were replaced by Rp 25 (i.e., 25 cm H_2O/L/s) [103]. The increased airflow resistance led to a longer time for the lung to fully exhale before starting a new breath (i.e., obstructive lung disease). To mimic a restrictive respiratory disease like fibrosis, the lung compliance was changed from the control setting of 0.1 L/cm H_2O (health: 0.05–0.1 L/cm H_2O) to 0.03 L/cm H_2O to simulate the higher lung stiffness [104–106].

Sar-Gel visualizations of the nebulized aerosol deposition are compared in Fig. 25.10b between the normal, asthmatic, and fibrosis cases for 30 respiration cycles [103]. The highest deposition in the upper airway was noted in the normal case, while the asthma case led to the least deposition in the upper airway. In comparison to the normal case, the slow inhalation in fibrosis gave rise to lower deposition in the mouth-throat region. It is noted that deposition patterns on the left and right walls were not symmetric for all of the three cases herein.

Figure 25.10c shows measured masses under the normal and pathological breathing conditions for 30 respiration cycles with each case repeating five times. The upper airway dose under asthmatic breathing conditions was significantly lower than (~50% of) the control case. By comparison, the fibrosis case led to similar doses as the control case. In light of the dose variability, no outlier existed in these three cases, suggesting good repeatability of the measured dosages. Figure 25.10d shows the subregional deposition in different regions of the airway cast, that is, the right upper,
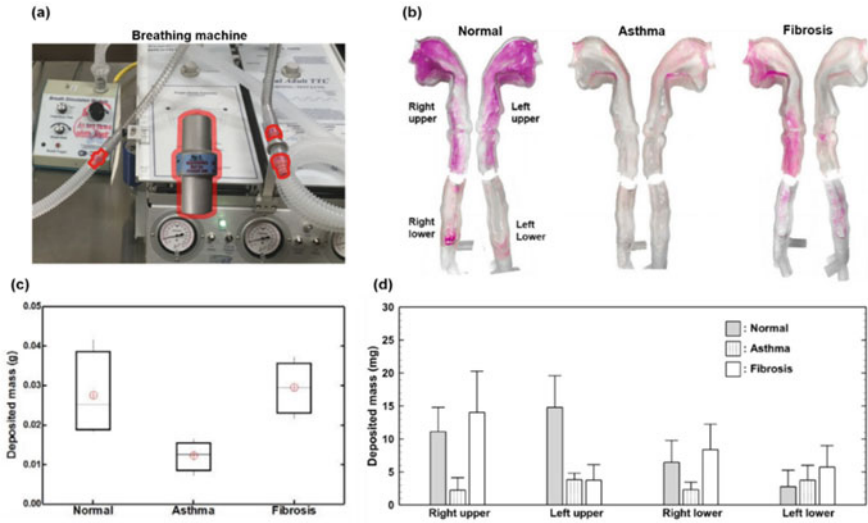
Fig. 25.10 Characterization of the deposition of aerosols from a mesh nebulizer in a mouth-lung cast under normal and pathological conditions: (**a**) PneuFlo parabolic flow resistor and their locations in the breathing machine; (**b**) surface deposition under three breathing conditions: normal, asthma, and fibrosis; (**c**) measured masses under the normal and pathological breathing conditions for 30 respiration cycles; and (**d**) deposited masses in the four subregions of the mouth-lung cast

left upper, right lower, and left lower. Apparently, the dosimetry of nebulized aerosols was highly sensitive to the breathing conditions. The asymmetric ventilations to the left and right lungs were presumably responsible for the left-right asymmetry in deposited doses. Again, the dosimetry variability was not significant with no obvious outliers, indicating satisfactory repeatability of the in vitro measurements.

25.3.3.4 Statistical Shape Modeling for Lung Morphing

Statistical shape modeling (SSM) has been demonstrated to be a useful method to study lung structural remodeling and resultant dosimetry variability. Even though SSM was originally developed as an algrothm in computer graphics and image processing [107, 108], it has been increasingly used in biomechanics, such as evaluation of fracture risks or implant performance [109, 110], face recognition [111], forensics [112], anthropology [113], and evolutional biology [114, 115]. SSM has been demonstrated to be an effective tool to evaluate a large number of subjects based on a limited number of original samples.

In theory, a training set was used to find the principal components (or eigenvectors/features) that were further used to generate new samples by varying the coefficients (or weights) of major eigenvectors. Figure 25.11a shows four examples of the SSM-generated lung models, which have a similar architecture as the training set but has a remodeled left lower lung lobe. The first two models
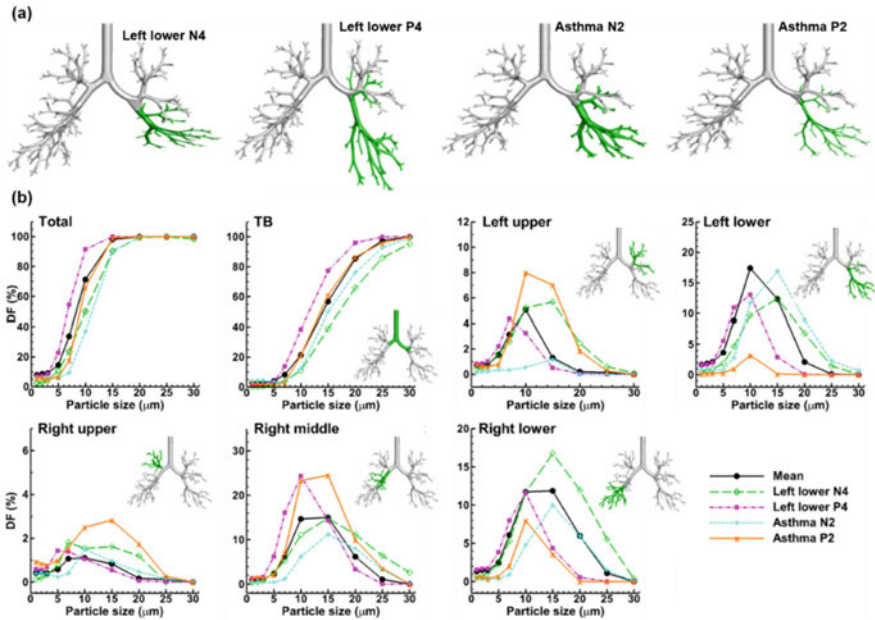
Fig. 25.11 Statistical shape modeling in morphing lung diseases and aerosol inhalation dosimetry: (**a**) four lung geometries generated from statistical shape modeling, with first two being rigid or over compliant and the last two being dilated and constricted, and (**b**) total and subregional deposition fractions (DFs) of the four remodeled geometries in comparison to the normal geometry. The numbers N2 and P2 represent the weights of the principal components (i.e., features) that reconstruct the two asthmatic lung models

represent the lungs with different compliances, while the last two models represent the over-inflation or constriction of the left lower lobe, respectively.

Figure 25.11b compares the doses between the normal and remodeled lung geometries. The highest total DF was predicted in the P4 model (pink solid squares in Fig. 25.11b), while the lowest total DF was predicted in the N2 model. Larger differences due to lung structural remodeling were observed in subregional DFs, as shown in the second to seventh panels in Fig. 25.11b. Moreover, large DF variations occurred not only in the regions with structural remodeling (i.e., the two left lobes), but also in the right upper and middle lobes, suggesting a systematic influence from local airway remodeling.

25.3.4 Nasal Drug Delivery

25.3.4.1 Deposition Visualization for Nasal Sprays and Nebulizers

Figure 25.12a visualizes the deposition of nasal sprays using Sar-Gel [2]. The plume angle of the sprays was $19° \pm 0.6°$, $35° \pm 0.8°$, $33° \pm 0.8°$, $20° \pm 0.5°$ for Miaoling, Astelin, Apotex, and Nasonex, respectively. It was observed that most spray droplets
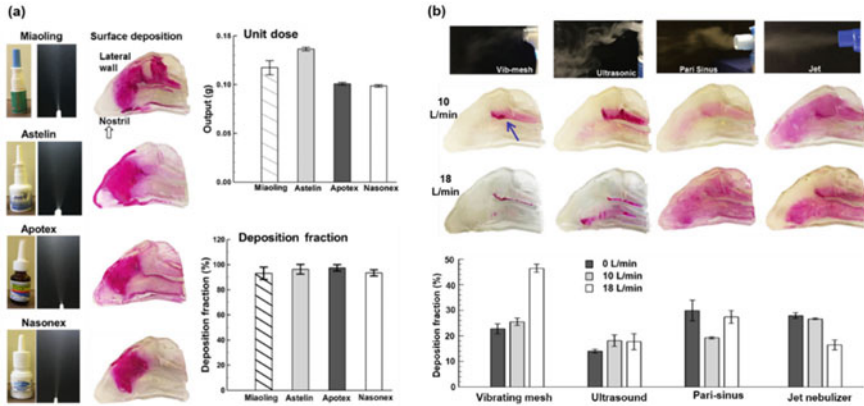
Fig. 25.12 In vitro tests of nasal sprays and nebulizers: (**a**) plumes, deposition patterns, and doses in the nose cast using different nasal spray products; (**b**) soft mists, deposition patterns, and deposition fractions of different types of nebulizers (i.e., vibrating mesh, ultrasound, Pari Sinus, and jet nebulizer)

deposited in the anterior nose, especially in the nasal valve region. The unit output (per stroke) of the nasal sprays is 0.12 ± 0.15 g. Close to 100% of the nasal sprays that were administered into the nostril(s) deposited inside the nose (right lower panel, Fig. 25.12a).

Figure 25.12b shows the Sar-Gel visualization of nasal deposition using four nebulizers of different mechanisms in the aerosol generation. The nozzle angle to the nostril was 60° from the horizontal direction. Low-speed soft mists were noted in all nebulizers except the jet nebulizer (upper right, Fig. 25.12b). Downward droplet motions occurred after discharging from the ultrasonic nebulizer due to the slow velocity and large size of the droplets. The deposition patterns were remarkably different among the four nebulizers (middle panel, Fig. 25.12b), from focused (mesh nebulizer) to widespread (jet-type) patterns. At a low inhalation rate (10 L/min), the strip of deposition on the edge of the middle turbinate (blue arrow) is consistent with the main inspiratory flow. At 18 L/min, more droplets were entrained by the main flow into the median passage, reducing the deposition on the turbinate edge. Considering the ultrasonic nebulizer, similar patterns were obtained at 10 and 18 L/min. Considering the Pari Sinus, the deposition distribution varied from less diffusive at 10 L/min to more widespread at 18 L/min. In the jet nebulizer, the highly dispersed deposition was found at both flow rates. Also, there was less deposition in the upper nose at 18 L/min. The core flow mainly occurred in the lower and median passages and entrained aerosols that otherwise went to the upper nose.

The lower panel of Fig. 25.12b shows the deposition fractions (DFs) at three respiration flow rates, with each test case being repeated five times. In comparison to the nasal spray products, the deposition of nebulized aerosols is much lower. The maximum DF is 46% for the mesh nebulizer at 18 L/min and the minimum DF is 15% for the ultrasonic nebulizer at 0 L/min (breath-holding). Interesting trends are

noted in the DF variation with flow rate for different nebulizers: the DF increases with flow rate for the mesh and ultrasonic nebulizer, while it decreases with flow rate for Pari Sinus and Philips jet nebulizers.

25.3.4.2 Normal Versus Bidirectional Nasal Drug Delivery

Different patterns of particle deposition are expected in the two passages under the bidirectional breathing pattern [116, 117]. To visualize the deposition pattern in the second passage, the direction of the bidirectional delivery was reversed, namely from "left in right out" to "right in left out" (Fig. 25.13a), so that particle deposition in the left (exiting) passage could be revealed. As expected, much fewer aerosols were deposited in the second passage. Figure 25.13b shows the deposition pattern after 1 minute's administration. This diminished deposition is reasonable considering that the majority of the administered droplets have been filtered out in the first (entrance) passage. Overall, the bidirectional technique yielded higher depositions in both the nasal cavity and the olfactory region compared to the normal technique. It is interesting to see from Fig. 25.13b that PARI Sinus performs better with the normal delivery method, while the mesh nebulizer is better with the bidirectional technique. This trend is valid in both the nasal cavity and the olfactory region.

To further understand the bidirectional effects on particle behaviors, snapshots of particle motion at various instants after administration were computed (Fig. 25.13c). The velocity vectors were also plotted on particles at selected instants. After 30 ms, particles approached the nasopharynx and changed directions sharply in the bi-directional mode to enter the second passage, leading to greater resistance than the normal mode. This increased resistance would affect the airflow and particle dynamics in both nasal passages, and the second passages in particular due to the ambient pressure at its exit. The diffusive surface deposition predicted by numerical
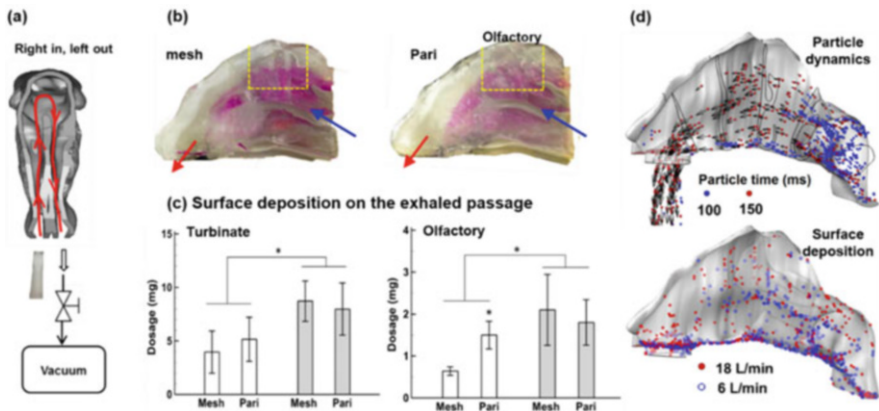

Fig. 25.13 Deposition pattern in the second (exiting) nasal passage using the bidirectional delivery protocol for the mesh (Voyager Pro) and PARI Sinus nebulizers: (**a**) delivery diagram (right in, left out), (**b**) deposition pattern, (**c**) deposition fractions in the turbinate and olfactory region, and (**d**) simulation results of the particle dynamics and deposition distribution in the exhaled passage

simulations (lower panel, Fig. 25.13c) is consistent with that obtained via in vitro tests (Fig. 25.13b).

25.3.4.3 Nasal Passage Dilation Effects

The human nose is a compliant structure that can change its shape/size either actively or passively to adjust airflow ventilation. Nasal expansion can alter the dosimetry of inhaled aerosols within the nasal cavity [118]. To quantify the dosimetry variation from nasal dilations, both in vitro tests and numerical simulations were undertaken in three nasal models (N0, N1, N2) with progressive dilation in the nasal passages (Fig. 25.14a, b). Specifically, gradual expansion was made to the nasal valve region, as evidenced by the front nose width of 2.49, 2.90, and 3.40 com in N0, N1, and N2, respectively (Fig. 25.14a). Relative to the control case N0, the expansion rate of the nasal valve was 30% and 50% in N1 and N2 (Fig. 25.14b).

First, valve dilation on flow partition in the nose was investigated. Both nasal valves were split into the upper and lower zones and their ventilation rates were quantified (Fig. 25.14c). In contrast to a similar upper-lower area ratio (~39%) for the three models, the flow ventilation to the upper zone was much lower, that is, 17–22%. Moreover, valve dilation enhanced the flow partition to the upper zone, which was 17% in N0 and 20% in N2 for the normal (unilateral) delivery and was 18.5% in N0 and 21% in N2 for the bidirectional delivery. The flow partition to the upper valve increased significantly in the left nose (the exhalation nasal passage) for the bidirectional delivery, with a 30.5% flow partition in N0 and 36% in N2. In
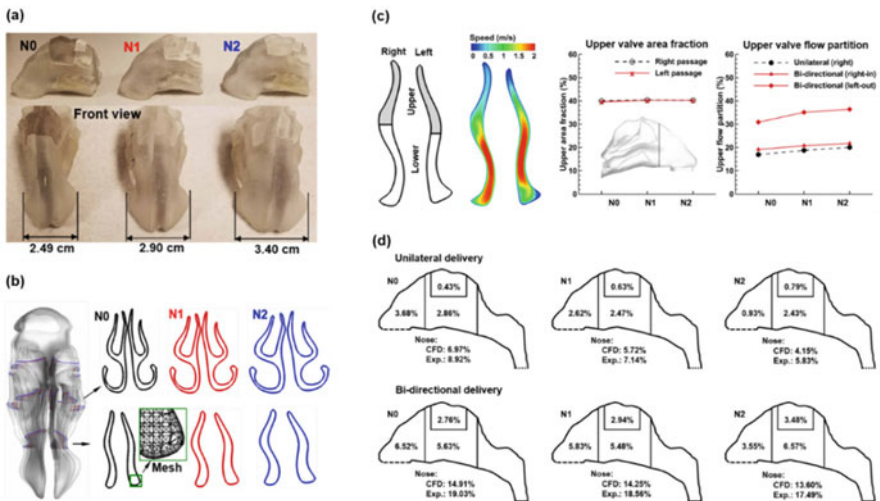

Fig. 25.14 Nasal passage dilation effects: (**a**) 3D-printed casts of three nasal models (N0, N1, N2) with increasing passage dilations, (**b**) cross-sections of the three nose dilatation models at the nasal valve and turbinate, (**c**) CFD-predicted flow partition, and (**d**) comparison of CFD and in vitro measured deposition fractions among the three models under unilateral and bidirectional deliveries

comparison to the right nose (inspiratory nasal passage), the high-speed flow zone in the left valve shifted upward, as demonstrated by the speed contour in Fig. 25.14c.

Numerically predicted DFs are shown in Fig. 25.14d for the three models in comparison to in vitro measurements. Good agreement was attained between the predicted and measured DFs both in magnitude and trend. The predicted DFs slightly, but consistently, underestimated the experimental data. For both delivery methods, the vestibular dosage decreased with the valve dilation. Specifically, a large decrease in the vestibular dosage occurred from N1 to N2 with the normal delivery method. On the other hand, the olfactory dosage increased with the valve dilation for all cases herein, which was 0.43%, 0.63%, and 0.79% in N0, N1, and N2, respectively. Further increased olfactory DFs were achieved using the bidirectional method, with the olfactory DF being 2.76%, 2.94%, and 3.48% in N0, N1, and N2, respectively. The optimal olfactory DF with bidirectional delivery (i.e., 3.48% in N2) was around four times the unilateral olfactory DF in N2 (0.79%) and eight times that in N0 (0.43%).

25.3.4.4 Targeted Olfactory Delivery Using Magnetic Guidance

To evaluate whether it is practical to use magnetic field to guide ferromagnetic particles to the olfactory region [99, 119], a two-plate channel with a 10-mm height and 150-mm length was tested with permanent magnets above the channel (Fig. 25.15a). The particle density was 1500 kg/m^3 as a mixture of drug and iron nanoparticles, the relative magnetic permeability of the particles was 700, and the particle size was 15 μm. Without a magnetic field, particles followed parabolic paths due to the gravity (Fig. 25.15a). By imposing an appropriate magnetic field, particle motions could be controlled, for instance, to move horizontally versus settling vertically (layout 1). Particles can also be guided to a specific site by imposing a strong attraction force locally (layout 2). The magnet field was nonuniform; it was
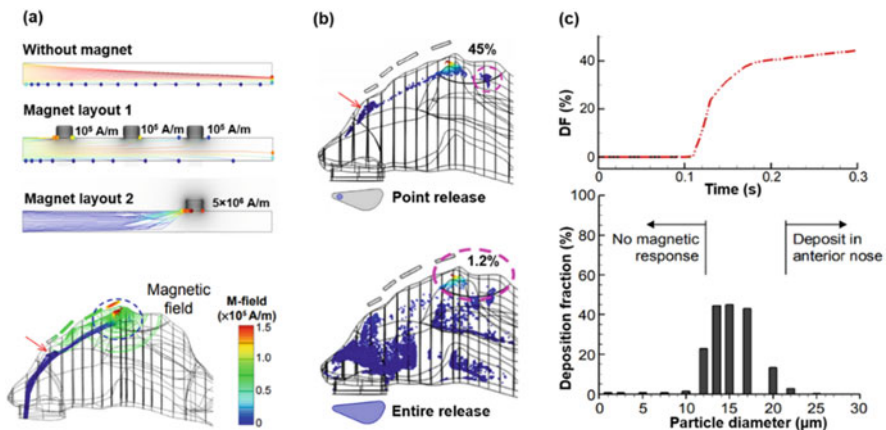
Fig. 25.15 Delivering magnetic particles to the olfactory region: (**a**) feasibility study in a two-plate channel, (**b**) point release of particles versus releasing particles from the entire nostril, and (**c**) olfactory dose as a function of the particle size

stronger near the magnet bars and decayed quickly away from the magnet bars. It was demonstrated that by releasing particles from a specific point (point release) and imposing a proper magnetic strength, the olfactory dose could be as high as 45% (Fig. 25.15b, c). By comparison, only 1.2% of particles could reach the olfactory region if being released from the entire nostril, even with an optimal magnetic strength (Fig. 25.15b).

The delivery efficiency of magnetic particles to the olfactory region is highly sensitive to the particle size. The most effective olfactory delivery occurred for particles of 10–20 μm. Decreased olfactory doses occurred for particles $\leq$10 μm or $\geq$20 μm. This is because that the particles $\leq$10 μm have low response to magnetic force, while particles $\geq$20 μm will be filtered out by the nasal valve from inertia impaction. Note that the magnetic force experienced by a particle varies with the third power of the particle size (d_p^3), in comparison to the first power of the magnetic intensity. The optimal olfactory dosimetry was shown to be 13–17 μm [99, 119].

25.3.4.5 Pulsating Aerosol Delivery to Maxillary Sinuses

The delivery efficiency of the drugs to the paranasal sinuses is unacceptably low at this stage. Pulsating flows have been shown to improve drug delivery into these secluded cavities due to flow-sinus resonance, but a manageable control on the delivery efficiency is still impractical. The maxillary sinuses are located peripherally at both sides of the nose and connected to the middle meatus through an ostium. To gain a better understanding of the pulsating aerosol delivery to the sinus, the variation of resonance frequency and sinus deposition with the ostium size, sinus shape, and pulsation frequency were systemically investigated [120]. The sinus model was built based on MRI head scans of a 53-year-old healthy male and connected to an existing nasal cavity model (Fig. 25.16a, b). To evaluate the geometrical effect of the sinus, the shape and size of the original sinus were modified using HyperMorph 10.0 (Troy, MI). Figure 25.16a shows the 3D-printed hollow casts of the sinuses with a 4-mm wall thickness (Fig. 25.16a).

To find the resonance frequencies of the nose-sinus geometry, a sampling point was specified in the ostium that connected the nasal cavity and the sinus. The variation of pressure (dashed line) and local acceleration (solid line) versus the input frequencies are shown in Fig. 25.16c for the sampling point. Two resonant frequencies are identified: 545 and 2260 Hz. Figure 25.16d shows the COMSOL-predicted sinus deposition in comparison to in vitro tests. As expected, the optimal sinus DF occurs at 545 Hz (resonant frequency) and decreases as the pulsating frequency drifts away from 545 Hz. The sinus DF changes insignificantly when varying the sinus dimensions as in this study.

Figure 25.16e shows the acoustic pressures in the nose-sinus ($D = 3$ mm, $L = 3$ mm, and Vol/Vol$_0 = 1$) at 545 Hz. A large pressure gradient was noted across the ostium. Figure 25.16f shows the distribution of the particle deposition within the sinus after 1 minute's pulsating drug delivery. Even though at a small amount, some particles indeed enter the sinus driven by the oscillating pressure waves (Fig. 25.16f), which have the largest amplitudes at the resonant frequency. Particles remaining inside the nasal passage are also dispersed by the acoustic waves
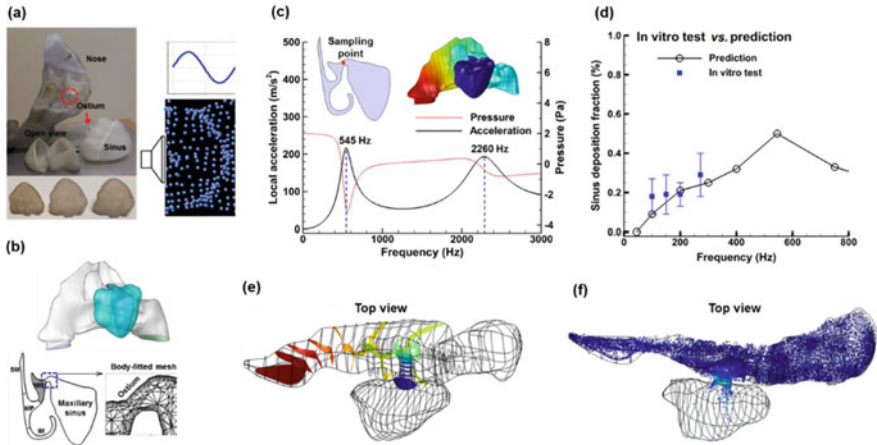
Fig. 25.16 Pulsating aerosol delivery to maxillary sinuses: (**a**) hollow casts of nose-sinus models, (**b**) computational model with near-wall prismatic mesh, (**c**) resonance occurs at 545 Hz, (**d**) comparison between in vitro measurements and numerical predictions, (**e**) acoustic pressure, and (**f**) sinus deposition distribution

(Fig. 25.16f). In light of the extremely low sinus dose at the current stage, further studies are needed in harnessing the pulsating aerosols. With a proper sound frequency and amplitude, it is promising to control the drug delivery to the paranasal sinuses or the olfactory region and achieve clinically relevant doses.

25.3.5 Computational Fluid-Particle Dynamics for COVID-19: Effect of Mask-Wearing

The year 2020 has witnessed several surges of COVID-19 pandemic in the USA and around the world. This pandemic has been caused by the SARS-CoV-2 virus, or coronavirus, and has been demonstrated to transmit from person to person through respiratory droplets and small particles, which are produced when an infected person speaks, breathes, coughs, or sneezes. These aerosols can be breathed into the respiratory tract and lead to infection. Community spread of COVID-19 has been reported frequently and is the major reason for COVID-transmission. Considering that the generation and transport of respiratory droplets share the same mechanisms of pharmaceutical aerosols, extensive studies have been undertaken since the pandemic to understand better the transmission routes and curb the transmission momentum. The example presented below demonstrated how computer-aided modeling and simulations added to our understanding of the effects of wearing a facemask on protection efficiencies.

In addition to social distancing and frequent handwashing, facemask-wearing has been an effective preventive measure to reduce viral community transmission. Wearing a mask both lower the inhalation of ambient virus-laden droplets and
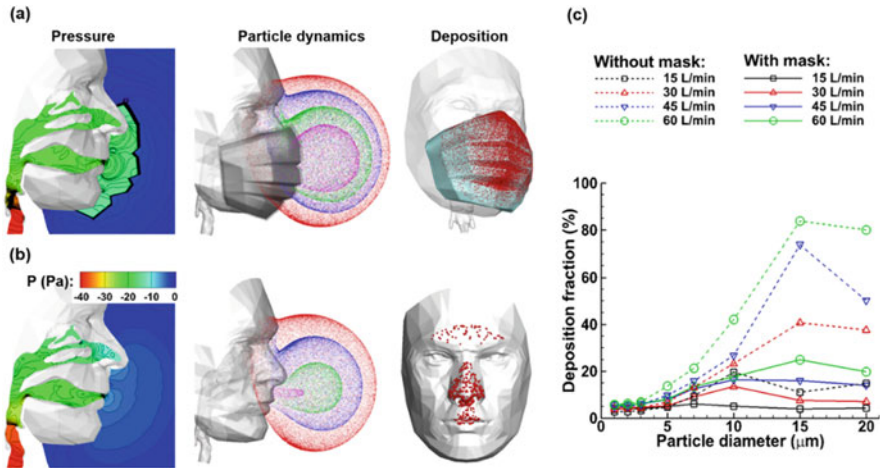
Fig. 25.17 Mask-wearing effects on respiration dynamics: (**a**) with a surgical mask, (**b**) without a mask, and (**c**) comparison of deposition of airborne aerosols with versus without a mask for different particle sizes and inhalation flow rates

minimize the exhalation of virus-laden droplets from a COVID patient [121, 122]. However, when talking about the facemask protective effectiveness, we often refer to the filtration efficiency of the mask material (like N95 being 95% effective), not the effectiveness it protects people from airborne bacteria/viruses. Till now, we do not have quantitative data on mask protection efficiencies when we wear them, which are more relevant to evaluate the risk and curb the COVID transmission [123, 124]. In this instance, we aimed to quantify the actual protection efficiencies to the upper airway when wearing a three-layer surgical mask [125].

To this aim, we developed a physiologically accurate model of a subject wearing a pleated surgical mask (Fig. 25.17a, b). Using numerical methods, we tracked aerosols through the facemask and studies their behavior and fates after crossing the facemask (Fig. 25.17a). Among these aerosol droplets, some will deposit on the face and the others will enter the airway. We further follow these droplets into the respiratory airway and find out where they will deposit, for instance, in the nose, pharynx, or into the lung. The protection efficiency of different regions of the airway can then be calculated (Fig. 25.17c).

The results may be surprising to many. Wearing an old or low-filtration mask (say <35%) can inhale more aerosol particles that are smaller than 2.5 μm (PM$_{2.5}$) [125]. Figure 25.17c compares the deposition fraction of airborne aerosol between wearing a 65%-filtration mask and with no mask. While good protection by mask was observed for particles >10 μm, equivalent deposition of 0–2.5 μm was predicted with and without a mask. It appears intuitive to premise that with a mask, regardless old or new, will always be better off than without a facemask. However, this premise is valid only for aerosols ≥5 μm, not for PM$_{2.5}$. The modified (slower) airflow when wearing a mask helps the particles to be inhaled into the nose. The filtration efficiency of a three-layer surgical mask can be any value between 25% (used) to

95% (new). While wearing a 95% mask will protect well, wearing a 25%-filtration mask can be worse than without [125]. Moreover, for environments with high concentrations of virus-laden $PM_{2.5}$ aerosols, such as COVID critical care units or COVID-specialized hospitals, face-covering with only a three-layer surgical mask would not provide enough protection.

25.4   Conclusion

In this chapter, we presented the fundamental theories in respiratory aerosol dynamics and demonstrated their usages through a series of efforts in our lab aiming to improve the physical realism of respiratory airway models. Both numerical and experimental tests were performed to this aim by exploring inhalation dosimetry in different regions of the airway (i.e., the mouth-throat, nose, and lung) and using different delivery techniques (i.e., normal vs. bidirectional nasal delivery, aerodynamic vs. magnetophoretic vs. acoustophoretic guidance, etc.). Specifically, computer-aided image-based design of the airway models opened a new door to the pharmaceutical industries to test the delivery efficiency and variability that was not even feasible less than 20 years ago. With anatomically accurate airway models and complementary numerical simulations, a better understanding has been attained in existing inhalation devices and delivery protocols, and improvements and optimization have been achieved in some cases. Furthermore, new devices or protocols can be designed for personalized diagnosis and targeted drug delivery.

25.5   Credible Online Resources for Further Reading

URL	Category of source	What to read or refer
https://www.ansys.com/products/fluids/ansys-fluent	Private company	Software to simulate airflow and particle deposition
https://www.ansys.com/services/training-center/fluids/introduction-to-ansys-icem-cfd	Private company	Tutorial for developing airway models, set up numerical simulations, and visualize results
https://www.altair.com/hypermesh	Private company	Software to change model morphology
https://www.comsol.com	Private company	Software to simulate Multiphysics phenomenon
https://www.comsol.com/models	Private company	Learn more about how to set up COMSOL simulations
https://www.slicer.org/	Open source	Software to segment medical images
https://www.slicer.org/wiki/Documentation/4.10/Training	Open source	Learn more about how to Slicer to process medical images
https://www.materialise.com	Private company	Software for image segmentation

References

1. Xi J, Longest PW (2007) Transport and deposition of micro-aerosols in realistic and simplified models of the oral airway. Ann Biomed Eng 35:560–581. https://doi.org/10.1007/s10439-006-9245-y

2. Xi J, Yuan JE, Zhang Y, Nevorski D, Wang Z, Zhou Y (2016) Visualization and quantification of nasal and olfactory deposition in a sectional adult nasal airway cast. Pharm Res 33:1527–1541. https://doi.org/10.1007/s11095-016-1896-2

3. Darquenne C, Fleming JS, Katz I, Martin AR, Schroeter J, Usmani OS et al (2016) Bridging the gap between science and clinical efficacy: physiology, imaging, and modeling of aerosols in the lung. J Aerosol Med 29:107–126. https://doi.org/10.1089/jamp.2015.1270

4. Xi J, Talaat M, Si XA, Han P, Dong H, Zheng S (2020) Alveolar size effects on nanoparticle deposition in rhythmically expanding-contracting terminal alveolar models. Comput Biol Med 121:103791. https://doi.org/10.1016/j.compbiomed.2020.103791

5. Talaat K, Xi J, Baldez P, Hecht A (2019) Radiation dosimetry of inhaled radioactive aerosols: CFPD and MCNP transport simulations of radionuclides in the lung. Sci Rep 9:1–21. https://doi.org/10.1038/s41598-019-54040-1

6. Zhang Z, Martonen TB (1997) Deposition of ultrafine aerosols in human tracheobronchial airways. Inhal Toxicol 9:99–110. https://doi.org/10.1080/089583797198295

7. Inthavong K, Tian ZF, Li HF, Tu JY, Yang W, Xue CL et al (2006) A numerical study of spray particle deposition in a human nasal cavity. Aerosol Sci Technol 40:1034–U1033. https://doi.org/10.1080/02786820600924978

8. Pharmacopeia US (2005) Physical tests and determinations: aerosols, nasal sprays, metered-dose inhalers, and dry powder inhalers. In: United States Pharmacopeia First Supplement, 28-NF, General Chapter (601), vol 28. United States Pharmacopeial Convention, Rockville, pp 3298–3316

9. Zhou Y, Sun J, Cheng Y-S (2011) Comparison of deposition in the USP and physical mouth-throat models with solid and liquid particles. J Aerosol Med Pulm Drug Deliv 24:277–284. https://doi.org/10.1089/jamp.2011.0882

10. Clark A, Newman S, Dasovich N (1998) Mouth and oropharyngeal deposition of pharmaceutical aerosols. J Aerosol Med 11:S116–S120. https://doi.org/10.1089/jam.1998.11.Suppl_1.S-116

11. Newman SP (1998) How well do in vitro particle size measurements predict drug delivery in vivo? J Aerosol Med Deposit Clear Eff Lung 11:S97–S104

12. Ali M, Mazumder MK, Martonen TB (2009) Measurements of electrodynamic effects on the deposition of MDI and DPI aerosols in a replica cast of human oral-pharyngeal-laryngeal airways. J Aerosol Med 22:35–44. https://doi.org/10.1089/jamp.2007.0637

13. Longest PW, Tian G, Walenga RL, Hindle M (2012) Comparing MDI and DPI aerosol deposition using In vitro experiments and a new stochastic individual path (SIP) model of the conducting airways. Pharm Res 29:1670–1688. https://doi.org/10.1007/s11095-012-0691-y

14. Burnell PKP, Asking L, Borgstrom L, Nichols SC, Olsson B, Prime D et al (2007) Studies of the human oropharyngeal airspaces using magnetic resonance imaging IV—the oropharyngeal retention effect for four inhalation delivery systems. J Aerosol Med Deposit Clear Eff Lung 20:269–281. https://doi.org/10.1089/jam.2007.0566

15. Cheng YS, Zhou Y, Chen BT (1999) Particle deposition in a cast of human oral airways. Aerosol Sci Technol 31:286–300. https://doi.org/10.1080/027868299304165

16. Golshahi L, Noga ML, Finlay WH (2012) Deposition of inhaled micrometer-sized particles in oropharyngeal airway replicas of children at constant flow rates. J Aerosol Sci 49:21–31. https://doi.org/10.1016/j.jaerosci.2012.03.001

17. Grgic B, Finlay WH, Burnell PKP, Heenan AF (2004) In vitro intersubject and intrasubject deposition measurements in realistic mouth-throat geometries. J Aerosol Sci 35:1025–1040. https://doi.org/10.1016/j.jaerosci.2004.03.003

18. Heenan AF, Finlay WH, Grgic B, Pollard A, Burnell PKP (2004) An investigation of the relationship between the flow field and regional deposition in realistic extra-thoracic airways. J Aerosol Sci 35:1013–1023. https://doi.org/10.1016/j.jaerosci.2004.03.004

19. Cheng KH, Cheng YS, Yeh HC, Swift DL (1997) Measurements of airway dimensions and calculation of mass transfer characteristics of the human oral passage. J Biomech Eng 119:476–482. https://doi.org/10.1115/1.2798296

20. Borgstrom L, Olsson B, Thorsson L (2006) Degree of throat deposition can explain the variability in lung deposition of inhaled drugs. J Aerosol Med 19:473–483. https://doi.org/10.1089/jam.2006.19.473

21. De Backer JW, Vos WG, Burnell P, Verhulst SL, Salmon P, De Clerck N et al (2009) Study of the variability in upper and lower airway morphology in Sprague-Dawley rats using modern micro-CT scan-based segmentation techniques. Anat Rec 292:720–727. https://doi.org/10.1002/ar.20877

22. Garcia GJM, Schroeter JD, Segal RA, Stanek J, Foureman GL, Kimbell JS (2009) Dosimetry of nasal uptake of water-soluble and reactive gases: a first study of interhuman variability. Inhal Toxicol 21:607–618. https://doi.org/10.1080/08958370802320186

23. Garcia GJM, Tewksbury EW, Wong BA, Kimbell JS (2009) Interindividual variability in nasal filtration as a function of nasal cavity geometry. J Aerosol Med Pulm Drug Deliv 22:139–155. https://doi.org/10.1089/jamp.2008.0713

24. Hofmann W, Asgharian B, Winkler-Heil R (2002) Modeling intersubject variability of particle deposition in human lungs. J Aerosol Sci 33:219–235. https://doi.org/10.1016/S0021-8502(01)00167-7

25. Schroeter JD, Garcia GJM, Kimbell JS (2010) A computational fluid dynamics approach to assess interhuman variability in hydrogen sulfide nasal dosimetry. Inhal Toxicol 22:277–286. https://doi.org/10.3109/08958370903278077

26. Thekedar B, Oeh U, Szymczak W, Hoeschen C, Paretzke HG (2011) Influences of mixed expiratory sampling parameters on exhaled volatile organic compound concentrations. J Breath Res 5:016001. https://doi.org/10.1088/1752-7155/5/1/016001

27. Vijverberg SJH, Koenderman L, Koster ES, van der Ent CK, Raaijmakers JAM, Maitland-van der Zee AH (2011) Biomarkers of therapy responsiveness in asthma: pitfalls and promises. Clin Exp Allergy 41:615–625. https://doi.org/10.1111/j.1365-2222.2011.03694.x

28. Longest PW, Xi J, Hindle M (2013) Effective delivery of nanoparticles and micrometer-sized pharmaceutical aerosols to the lung through enhanced condensational growth. U.S. patent number: 5522385

29. Xi J, Kim J, Si XA, Zhou Y (2013) Diagnosing obstructive respiratory diseases using exhaled aerosol fingerprints: a feasibility study. J Aerosol Sci 64:24–36. https://doi.org/10.1016/j.jaerosci.2013.06.003

30. Xi J, Yang T (2019) Variability in oropharyngeal airflow and aerosol deposition due to changing tongue positions. J Drug Deliv Sci Technol 49:674–682. https://doi.org/10.1016/j.jddst.2019.01.006

31. Xi J, Si XA, Kim JW (2015) Characterizing respiratory airflow and aerosol condensational growth in children and adults using an imaging-CFD approach. In: Heat transfer and fluid flow in biological processes. Academic, pp 125–155

32. Xi J, Kim J, Si XA (2016) Effects of nostril orientation on airflow dynamics, heat exchange, and particle depositions in human noses. Eur J Mech B/Fluids 55:215–228

33. Cheng KH, Cheng YS, Yeh HC, Swift DL (1997) An experimental method for measuring aerosol deposition efficiency in the human oral airway. Am Ind Hyg Assoc J 58:207–213. https://doi.org/10.1080/15428119791012856

34. Stapleton KW, Guentsch E, Hoskinson MK, Finlay WH (2000) On the suitability of k-epsilon turbulence modeling for aerosol deposition in the mouth and throat: a comparison with experiment. J Aerosol Sci 31:739–749. https://doi.org/10.1016/S0021-8502(99)00547-9

35. DeHaan WH, Finlay WH (2004) Predicting extrathoracic deposition from dry powder inhalers. J Aerosol Sci 35:309–331. https://doi.org/10.1016/j.jaerosci.2003.09.002

36. Xi J, Longest PW (2008) Effects of oral airway geometry characteristics on the diffusional deposition of inhaled nanoparticles. J Biomech Eng 130:011008

37. Cheng YS, Yazzie D, Gao J, Muggli D, Etter J, Rosenthal GJ (2003) Particle characteristics and lung deposition patterns in a human airway replica of a dry powder formulation of polylactic acid produced using supercritical fluid technology. J Aerosol Med Deposit Clear Eff Lung 16:65–73. https://doi.org/10.1089/089426803764928374

38. Cheng YS, Fu CS, Yazzie D, Zhou Y (2001) Respiratory deposition patterns of salbutamol pMDI with CFC and HFA-134a formulations in a human airway replica. J Aerosol Med 14: 255–266. https://doi.org/10.1089/08942680152484180

39. Xi J, Berlinski A, Zhou Y, Greenberg B, Ou X (2012) Breathing resistance and ultrafine particle deposition in nasal–laryngeal airways of a newborn, an infant, a child, and an adult. Ann Biomed Eng 40:2579–2595. https://doi.org/10.1007/s10439-012-0603-7

40. Segal R, Kepler GM, Kalisak DL, Richardson RB, Kimbell JS (2003) Effects of differences in nasal anatomy on airflow distribution: a comparison of three individuals. Toxicol Sci 72:37–38. https://doi.org/10.1007/s10439-008-9556-2

41. Segal RA, Kepler GM, Kimbell JS (2008) Effects of differences in nasal anatomy on airflow distribution: a comparison of four individuals at rest. Ann Biomed Eng 36:1870–1882. https://doi.org/10.1007/s10439-008-9556-2

42. Miyawaki S, Hoffman EA, Wenzel SE, Lin C-L (2019) Aerosol deposition predictions in computed tomography-derived skeletons from severe asthmatics: a feasibility study. Clin Biomech 66:81–87. https://doi.org/10.1016/j.clinbiomech.2017.10.020

43. Choi J, Hoffman EA, Lin C-L, Milhem MM, Tessier J, Newell JD Jr (2017) Quantitative computed tomography determined regional lung mechanics in normal nonsmokers, normal smokers and metastatic sarcoma subjects. PLoS One 12:e0179812–e0179812. https://doi.org/10.1371/journal.pone.0179812

44. Miyawaki S, Hoffman EA, Lin C-L (2017) Numerical simulations of aerosol delivery to the human lung with an idealized laryngeal model, image-based airway model, and automatic meshing algorithm. Comput Fluids 148:1–9. https://doi.org/10.1016/j.compfluid.2017.02.008

45. Wu D, Tawhai MH, Hoffman EA, Lin C-L (2014) A numerical study of heat and water vapor transfer in MDCT-based human airway models. Ann Biomed Eng 42:2117–2131. https://doi.org/10.1007/s10439-014-1074-9

46. Lambert AR, O'Shaughnessy PT, Tawhai MH, Hoffman EA, Lin C-L (2011) Regional deposition of particles in an image-based airway model: large-Eddy simulation and left-right lung ventilation asymmetry. Aerosol Sci Technol 45:11–25. https://doi.org/10.1080/02786826.2010.517578

47. Kleinstreuer C, Zhang Z (2003) Laminar-to-turbulent fluid-particle flows in a human airway model. Int J Multiph Flow 29:271–289. https://doi.org/10.1016/S0301-9322(02)00131-3

48. Zhang Y, Finlay WH, Matida EA (2004) Particle deposition measurements and numerical simulations in a highly idealized mouth-throat. J Aerosol Sci 35:789–803. https://doi.org/10.1016/j.jaerosci.2003.12.006

49. Delvadia RR, Longest PW, Hindle M, Byron PR (2013) In vitro tests for aerosol deposition. III: effect of inhaler insertion angle on aerosol deposition. J. Aerosol Med 26: 145–156. https://doi.org/10.1089/jamp.2012.0989

50. Delvadia R, Hindle M, Longest PW, Byron PR (2013) In vitro tests for aerosol deposition II: IVIVCs for different dry powder inhalers in normal adults. J Aerosol Med 26:138–144. https://doi.org/10.1089/jamp.2012.0975

51. Zhou Y, Guo M, Xi J, Irshad H, Cheng Y-S (2014) Nasal deposition in infants and children. J Aerosol Med 27:110–116. https://doi.org/10.1089/jamp.2013.1039

52. Zhou Y, Xi J, Simpson J, Irshad H, Cheng Y-S (2013) Aerosol deposition in a nasopharyngolaryngeal replica of a 5-year-old child. Aerosol Sci Technol 47:275–282. https://doi.org/10.1080/02786826.2012.749341

53. Valentine R, Athanasiadis T, Thwin M, Singhal D, Weitzel EK, Wormald PJ (2008) A prospective controlled trial of pulsed nasal nebulizer in maximally dissected cadavers. Am J Rhinol Allergy 22:390–394. https://doi.org/10.2500/ajr.2008.22.3191

54. Moller W, Schuschnig U, Celik G, Munzing W, Bartenstein P, Haussinger K et al (2013) Topical drug delivery in chronic rhinosinusitis patients before and after sinus surgery using pulsating aerosols. PLoS One 8:e74991. https://doi.org/10.1371/journal.pone.0074991

55. Djupesland PG, Skretting A, Winderen M, Holand T (2006) Breath actuated device improves delivery to target sites beyond the nasal valve. Laryngoscope 116:466–472. https://doi.org/10.1097/01.mlg.0000199741.08517.99

56. Washington N, McGlashan JA, Jackson SJ, Bush D, Pitt KG, Rawlins DA et al (2000) The effect of nasal patency on the clearance of radiolabeled saline in healthy volunteers. Pharm Res 17:733–736. https://doi.org/10.1023/a:1007590501540

57. Suman JD, Laube BL, Lin TC, Brouet G, Dalby R (2002) Validity of in vitro tests on aqueous spray pumps as surrogates for nasal deposition. Pharm Res 19:1–6. https://doi.org/10.1023/a:1013643912335

58. Guo Y, Laube B, Dalby R (2005) The effect of formulation variables and breathing patterns on the site of nasal deposition in an anatomically correct model. Pharm Res 22:1871–1878. https://doi.org/10.1007/s11095-005-7391-9

59. Laube BL, Sharpless G, Shermer C, Nasir O, Sullivan V, Powell K (2010) Deposition of albuterol aerosol generated by pneumatic nebulizer in the Sophia Anatomical Infant Nose-Throat (SAINT) model. Pharm Res 27:1722–1725. https://doi.org/10.1007/s11095-010-0171-1

60. Fleming JS, Conway JH, Bolt L, Holgate ST (2003) A comparison of planar scintigraphy and SPECT measurement of total lung deposition of inhaled aerosol. J Aerosol Med 16:9–19. https://doi.org/10.1089/089426803764928310

61. Bondesson E, Bengtsson T, Borgstrom L, Nilsson LE, Norrgren K, Trofast E et al (2003) Planar gamma scintigraphy—points to consider when quantifying pulmonary dry powder aerosol deposition. Int J Pharm 258:227–240. https://doi.org/10.1016/s0378-5173(02)00579-3

62. Kundoor V, Dalby RN (2010) Assessment of nasal spray deposition pattern in a silicone human nose model using a color-based method. Pharm Res 27:30–36. https://doi.org/10.1007/s11095-009-0002-4

63. Kundoor V, Dalby RN (2011) Effect of formulation- and administration-related variables on deposition pattern of nasal spray pumps evaluated using a nasal cast. Pharm Res 28:1895–1904. https://doi.org/10.1007/s11095-011-0417-6

64. Courrier HM, Butz N, Vandamme TF (2002) Pulmonary drug delivery systems: recent developments and prospects. Crit Rev Ther Drug Carrier Syst 19:425–498. https://doi.org/10.1615/CritRevTherDrugCarrierSyst.v19.i45.40

65. Labiris NR, Dolovich MB (2003) Pulmonary drug delivery. Part I: physiological factors affecting therapeutic effectiveness of aerosolized medications. Br J Clin Pharmacol 56:588–599. https://doi.org/10.1046/j.1365-2125.2003.01892.x

66. Chan HK, Chew NY (2003) Novel alternative methods for the delivery of drugs for the treatment of asthma. Adv Drug Deliv Rev 55:793–805. https://doi.org/10.1016/s0169-409x(03)00078-4

67. Agertoft L, Pedersen S, Nikander K (1999) Drug delivery from the Turbuhaler and Nebuhaler pressurized metered dose inhaler to various age groups of children with asthma. J Aerosol Med 12:161–169. https://doi.org/10.1089/jam.1999.12.161

68. Gibson PG, Wlodarczyk JH, Borgas T (1995) Drug delivery in asthma: a comparison of spacers with a jet nebuliser. Aust N Z J Med 25:324–325. https://doi.org/10.1111/j.1445-5994.1995.tb01897.x

69. Si XA, Xi J, Kim J, Zhou Y, Zhong H (2013) Modeling of release position and ventilation effects on olfactory aerosol drug delivery. Respir Physiol Neurobiol 186:22–32. https://doi.org/10.1016/j.resp.2012.12.005

70. Kim J, Xi J, Si X, Berlinski A, Su WC (2014) Hood nebulization: effects of head direction and breathing mode on particle inhalability and deposition in a 7-month-old infant model. J Aerosol Med Pulm Drug Deliv 27:209–218. https://doi.org/10.1089/jamp.2013.1051

71. Xi J, Kim J, Si XA, Corley RA, Kabilan S, Wang S (2015) CFD modeling and image analysis of exhaled aerosols due to a growing bronchial tumor: towards non-invasive diagnosis and treatment of respiratory obstructive diseases. Theranostics 5:443–455. https://doi.org/10.7150/thno.11107

72. Easley SK, Pal S, Tomaszewski PR, Petrella AJ, Rullkoetter PJ, Laz PJ (2007) Finite element-based probabilistic analysis tool for orthopaedic applications. Comput Methods Programs Biomed 85:32–40. https://doi.org/10.1016/j.cmpb.2006.09.013

73. Laz PJ, Browne M (2010) A review of probabilistic analysis in orthopaedic biomechanics. Proc Inst Mech Eng H 224:927–943

74. Lu J, Xi J, Langenderfer JE (2017) Sensitivity analysis and uncertainty quantification in pulmonary drug delivery of orally inhaled pharmaceuticals. J Pharm Sci 106:3303–3315. https://doi.org/10.1016/j.xphs.2017.06.011

75. Guo C, Doub WH, Kauffman JF (2010) Propagation of uncertainty in nasal spray in vitro performance models using Monte Carlo simulation: part II. Error propagation during product performance modeling. J Pharm Sci 99:3572–3578. https://doi.org/10.1002/jps.22094

76. Guilmette RA, Wicks JD, Wolff RK (1989) Morphometry of human nasal airways in vivo using Magnetic Resonance Imaging. J Aerosol Med 2:365–377. https://doi.org/10.1089/jam.1989.2.365

77. Guilmette RA, Cheng YS, Yeh HC, Swift DL (1994) Deposition of 0.005–12 micrometer monodisperse particls in a computer-milled, MRI-based nasal airway replica. Inhal Toxicol 6 (Suppl 1):395–399

78. Cheng KH, Cheng YS, Yeh HC, Swift DL (1995) Deposition of ultrafine aerosols in the head airways during natural breathing and during simulated breath-holding using replicate human upper airway casts. Aerosol Sci Technol 23:465–474. https://doi.org/10.1080/02786829508965329

79. Kelly JT, Asgharian B, Kimbell JS, Wong B (2004) Particle depositon in human nasal airway replicas manufactured by different methods. Part II: ultrafine particles. Aerosol Sci Technol 38:1072–1079. https://doi.org/10.1080/027868290883432

80. Kelly JT, Asgharian B, Kimbell JS, Wong B (2004) Particle depositon in human nasal airway replicas manufactured by different methds. Part I: inertial regime particles. Aerosol Sci Technol 38:1063–1071. https://doi.org/10.1080/027868290883360

81. Schroeter JD, Kimbell JS, Asgharian B (2006) Analysis of particle deposition in the turbinate and olfacotry regions using a human nasal computational fluid dynamics model. J Aerosol Med 19:301–313. https://doi.org/10.1089/jam.2006.19.301

82. Shi H, Kleinstreuer C, Zhang Z (2006) Laminar airflow and nanoparticle or vapor deposition in a human nasal cavity model. J Biomech Eng 128:697–706. https://doi.org/10.1115/1.2244574

83. Xi J, Longest PW (2008) Numerical predictions of submicrometer aerosol deposition in the nasal cavity using a novel drift flux approach. Int J Heat Mass Transf 51:5562–5577. https://doi.org/10.1016/j.ijheatmasstransfer.2008.04.037

84. Si X, Xi J, Kim J (2013) Effect of laryngopharyngeal anatomy on expiratory airflow and submicrometer particle deposition in human extrathoracic airways. Open J Fluid Dyn 3:286–301. https://doi.org/10.4236/ojfd.2013.34036

85. Kim J, Xi J, Si XA (2013) Dynamic growth and deposition of hygroscopic aerosols in the nasal airway of a 5-year-old child. Int J Numer Method Biomed Eng 29:17–39. https://doi.org/10.1002/cnm.2490

86. Cohen BS, Asgharian B (1990) Deposition of ultrafine particles in the upper airways: an empirical analysis. J Aerosol Sci 21:789–797. https://doi.org/10.1016/0021-8502(90)90044-X

87. Xi J, Si X, Kim J, Su G, Dong H (2014) Modeling the pharyngeal anatomical effects on breathing resistance and aerodynamically generated sound. Med Biol Eng Comput 52:567–577

88. Morsi SA, Alexander AJ (1972) An investigation of particle trajectories in two-phase flow systems. J Fluid Mech 55:193–208. https://doi.org/10.1016/j.mvr.2010.05.002

89. Xi J, Longest PW (2009) Characterization of submicrometer aerosol deposition in extrathoracic airways during nasal exhalation. Aerosol Sci Technol 43:808–827. https://doi.org/10.1007/s10439-008-9552-6

90. Ribeiro P, Si X (2012) Section 2: electric and magnetic circuit. In: Beaty HW, Fink DG (eds) Standard handbook for electrical engineering, 16th edn. McGraw Hill, pp 2.1–2.58

91. Gao Y, Jian YC, Zhang LF, Huang JP (2007) Magnetophoresis of nonmagnetic particles in ferrofluids. J Phys Chem C 111:10785–10791. https://doi.org/10.1021/jp0705673

92. Settnes M, Bruus H (2012) Forces acting on a small particle in an acoustical field in a viscous fluid. Phys Rev E 85:016327

93. Xi J, Si X, Kim JW, Berlinski A (2011) Simulation of airflow and aerosol deposition in the nasal cavity of a 5-year-old child. J Aerosol Sci 42:156–173

94. Xi J, Si X, Longest WJP (2014) Electrostatic charge effects on pharmaceutical aerosol deposition in human Nasal–Laryngeal airways. Pharmaceutics 6:26–35

95. Rygg A, Longest W (2016) Absorption and clearance of pharmaceutical aerosols in the human nose: development of a CFD model. J Aerosol Med 29:416–431. https://doi.org/10.1089/jamp.2015.1252

96. Graham LJ, Taillon R, Mullin J, Wigle T (2010) Pharmaceutical process/equipment design methodology case study: cyclone design to optimize spray-dried-particle collection efficiency. Comput Chem Eng 34:1041–1048. https://doi.org/10.1016/j.compchemeng.2010.04.004

97. Si XA, Xi J (2016) Modeling and simulations of olfactory drug delivery with passive and active controls of nasally inhaled pharmaceutical aerosols. J Vis Exp e53902. https://doi.org/10.3791/53902

98. Xi J, Si X, Gaide R (2014) Electrophoretic particle guidance significantly enhances olfactory drug delivery: a feasibility study. PLoS One 9:e86593. https://doi.org/10.1371/journal.pone.0086593

99. Xi J, Zhang Z, Si XA, Yang J, Deng W (2016) Optimization of magnetophoretic-guided drug delivery to the olfactory region in a human nose model. Biomech Model Mechanobiol 15:877–891. https://doi.org/10.1007/s10237-015-0730-9

100. Xi J, Yuan JE, Yang M, Si X, Zhou Y, Cheng Y-S (2016) Parametric study on mouth–throat geometrical factors on deposition of orally inhaled aerosols. J Aerosol Sci 99:94–106. https://doi.org/10.1016/j.jaerosci.2016.01.014

101. Preacher KJ, Curran PJ, Bauer DJ (2006) Computational tools for probing interactions in multiple linear regression, multilevel modeling, and latent curve analysis. J Educ Behav Stat 31:437–448. https://doi.org/10.3102/10769986031004437

102. Xi J, Yang T, Talaat K, Wen T, Zhang Y, Klozik S et al (2018) Visualization of local deposition of nebulized aerosols in a human upper respiratory tract model. J Vis 21:225–237. https://doi.org/10.1007/s12650-017-0456-0

103. Wells B, Guest N, Martinez J, Hakizimana E, Si X, Su W et al (2018) Visualization and quantification of nebulized aerosol deposition in mouth-lung casts under healthy and abnormal breathing conditions. Lungs Breath 2:1–6. https://doi.org/10.15761/LBJ.1000127

104. Bernasconi M, Ploysongsang Y, Gottfried SB, Milic-Emili J, Rossi A (1988) Respiratory compliance and resistance in mechanically ventilated patients with acute respiratory failure. Intensive Care Med 14:547–553. https://doi.org/10.1007/bf00263528

105. Storstein O, Field AS Jr, Massumi R, Gray FD Jr (1959) Airway resistance and lung compliance; the effects of histamine and hyperventilation in normal subjects and patients with chronic lung disease. Yale J Biol Med 31:387–396

106. Papandrinopoulou D, Tzouda V, Tsoukalas G (2012) Lung compliance and chronic obstructive pulmonary disease. Pulm Med 2012:542769. https://doi.org/10.1155/2012/542769

107. Mardia KV, Kent JT, Walder AN (1991) Statistical shape models in image analysis. Comput Sci Stat 550–557
108. Slice DE (2007) Geometric morphometrics. Annu Rev Anthropol 36:261–281. https://doi.org/10.1146/annurev.anthro.34.081804.120613
109. Fitzpatrick C, FitzPatrick D, Lee J, Auger D (2007) Statistical design of unicompartmental tibial implants and comparison with current devices. Knee 14:138–144. https://doi.org/10.1016/j.knee.2006.11.005
110. Castro-Mateos I, Pozo JM, Cootes TF, Wilkinson JM, Eastell R, Frangi AF (2014) Statistical shape and appearance models in osteoporosis. Curr Osteoporos Rep 12:163–173. https://doi.org/10.1007/s11914-014-0206-3
111. Maghari AYA, Liao IY, Belaton B (2012) Quantitative analysis on PCA-based statistical 3D face shape modeling. In: Computational modelling of objects represented in images: fundamentals, methods and applications Iii. pp 13–18
112. Hauser R, Smolinski J, Gos T (2005) The estimation of stature on the basis of measurements of the femur. Forensic Sci Int 147:185–190. https://doi.org/10.1016/j.forsciint.2004.09.070
113. Krishan K, Chatterjee PM, Kanchan T, Kaur S, Baryah N, Singh RK (2016) A review of sex estimation techniques during examination of skeletal remains in forensic anthropology casework. Forensic Sci Int 261:165.e161–165.e168. https://doi.org/10.1016/j.forsciint.2016.02.007
114. Sella G, Hirsh AE (2005) The application of statistical physics to evolutionary biology. Proc Natl Acad Sci U S A 102:9541–9546. https://doi.org/10.1073/pnas.0501865102
115. Macdonald-Wallis C (2014) Statistical analysis of human growth and development. Int J Epidemiol 43:635–636. https://doi.org/10.1093/ije/dyu068
116. Xi J, Yuan J, Alshaiba M, Cheng D, Firlit Z, Johnson A, Nolan A, Su W (2016) Design and testing of electric-guided delivery of charged particles to the olfactory region: experimental and numerical studies. Curr Drug Deliv 13:265–274. https://doi.org/10.2174/1567201812666150909093050
117. Xi J, Wang Z, Nevorski D, White T, Zhou Y (2017) Nasal and olfactory deposition with normal and bidirectional intranasal delivery techniques: in vitro tests and numerical simulations. J Aerosol Med 30:118–131. https://doi.org/10.1089/jamp.2016.1295
118. Xi J, Wang Z, Si XA, Zhou Y (2018) Nasal dilation effects on olfactory deposition in unilateral and bi-directional deliveries: in vitro tests and numerical modeling. Eur J Pharm Sci 118:113–123. https://doi.org/10.1016/j.ejps.2018.03.027
119. Xi J, Zhang Z, Si X (2015) Improving intranasal delivery of neurological nanomedicine to the olfactory region using magnetophoretic guidance of microsphere carriers. Int J Nanomed 10:1211–1222. https://doi.org/10.2147/IJN.S77520
120. Xi J, Si XA, Peters S, Nevorski D, Wen T, Lehman M (2017) Understanding the mechanisms underlying pulsating aerosol delivery to the maxillary sinus: in vitro tests and computational simulations. Int J Pharm 520:254–266. https://doi.org/10.1016/j.ijpharm.2017.02.017
121. Gandhi M, Havlir D et al (2020) Open Forum Infect Dis 7:ofaa131. https://doi.org/10.1093/ofid/ofaa131
122. Eikenberry SE, Mancuso M, Iboi E, Phan T, Eikenberry K, Kuang Y et al (2020) To mask or not to mask: modeling the potential for face mask use by the general public to curtail the COVID-19 pandemic. Infect Dis Model 5:293–308. https://doi.org/10.1016/j.idm.2020.04.001
123. Asadi S, Cappa CD, Barreda S, Wexler AS, Bouvier NM, Ristenpart WD (2020) Efficacy of masks and face coverings in controlling outward aerosol particle emission from expiratory activities. Sci Rep 10:15665. https://doi.org/10.1038/s41598-020-72798-7
124. Liu Z, Yu D, Ge Y, Wang L, Zhang J, Li H et al (2019) Understanding the factors involved in determining the bioburdens of surgical masks. Ann Transl Med 7:754–754. https://doi.org/10.21037/atm.2019.11.91
125. Xi J, Si X, Nagarajan R (2020) Effects of mask-wearing on the inhalability and deposition of airborne SARS-CoV-2 aerosols in human upper airway. Phys Fluids 32:123312. https://doi.org/10.1063/5.0034580